PHYSICAL REVIEW D **94,** 054005 (2016)

Landau gauge Yang-Mills correlation functions

Anton K. Cyrol,[1] Leonard Fister,[2] Mario Mitter,[1] Jan M. Pawlowski,[1,3] and Nils Strodthoff[1,4]
[1]*Institut für Theoretische Physik, Universität Heidelberg, Philosophenweg 16, 69120 Heidelberg, Germany*
[2]*Institut de Physique Théorique, CEA Saclay, F-91191 Gif-sur-Yvette, France*
[3]*ExtreMe Matter Institute EMMI, GSI, Planckstrasse 1, D-64291 Darmstadt, Germany*
[4]*Nuclear Science Division, Lawrence Berkeley National Laboratory, Berkeley, California 94720, USA*
(Received 20 May 2016; published 6 September 2016)

We investigate Landau gauge $SU(3)$ Yang-Mills theory in a systematic vertex expansion scheme for the effective action with the functional renormalization group. Particular focus is put on the dynamical creation of the gluon mass gap at nonperturbative momenta and the consistent treatment of quadratic divergences. The nonperturbative ghost and transverse gluon propagators as well as the momentum-dependent ghost-gluon, three-gluon and four-gluon vertices are calculated self-consistently with the classical action as the only input. The apparent convergence of the expansion scheme is discussed and within the errors, our numerical results are in quantitative agreement with available lattice results.

DOI: 10.1103/PhysRevD.94.054005

I. INTRODUCTION

The past two decades have seen tremendous progress in the description of QCD with functional approaches such as the functional renormalization group (FRG), Dyson-Schwinger equations (DSE), and n-particle irreducible methods (nPI). These approaches constitute *ab initio* descriptions of QCD in terms of quark and gluon correlation functions. The full correlation functions satisfy a hierarchy of loop equations that are derived from the functional FRG, DSE and nPI relations for the respective generating functionals. By now, systematic computational schemes are available, which can be controlled by apparent convergence. In the present work on pure Yang-Mills (YM) theory we complement the work in quenched QCD [1], where such a systematic expansion scheme has been put forward within the FRG. Equipped with such a controlled expansion, functional approaches to QCD are specifically interesting at finite temperatures and large density, where reliable *ab initio* theoretical predictions and experimental results are missing at present.

Most progress with functional approaches has been made in Landau gauge QCD, which has many convenient properties for nonperturbative numerical computations. Applications of functional methods include the first-ever calculation of qualitative nonperturbative Landau gauge propagators as well as investigations of the phase structure of QCD. For reviews see [2–13], for applications to Yang-Mills theory see e.g. [14–24], and e.g. [25] for related studies in the Coulomb gauge. The formal, algebraic, and numerical progress of the past decades sets the stage for a systematic vertex expansion scheme of Landau gauge QCD. Quantitative reliability is then obtained with apparent convergence [1] as well as further systematic error controls inherent to the method, see e.g. [5,26–29]. In the aforementioned quenched QCD investigation [1], the gluon propagator was taken from a separate FRG calculation in [9,30]. This gluon propagator shows quantitative agreement with the lattice results, but has been obtained within an incomplete vertex expansion scheme. Therefore, the results [9,30] for the YM correlations functions give no access to systematic error estimates. In general, many applications of functional methods to bound states and the QCD phase diagram use such mixed approaches, where part of the correlation functions is deduced from phenomenological constraints or other external input. Despite the huge success of mixed approaches, a full *ab initio* method is wanted for some of the most pressing open questions of strongly interacting matter. The phase structure of QCD at large density is dominated by fluctuations and even a partial phenomenological parameter fixing at vanishing density is bound to lead to large systematic errors [31]. The same applies to the details of the hadron spectrum, in particular with regard to the physics of the higher resonances, which requires knowledge about correlation functions deep in the complex plane.

In the present work we perform a systematic vertex expansion of the effective action of Landau gauge YM theory within the functional renormalization group approach, discussed in Sec. II. The current approximation is summarized in Sec. II B, which also includes a comparison to approximations used in other works. This *ab initio* approach starts from the classical action. Therefore the only parameter is the strong coupling constant α_s at a large, perturbative momentum scale. The most distinct feature of YM theory is confinement, which is reflected by the creation of a gluon mass gap in Landau gauge. We discuss the necessity of consistent infrared irregularities as well as mechanisms for the generation of a mass gap in Sec. III. Numerical results from a

parameter-free, self-consistent calculation of propagators and vertices are presented in Sec. IV. Particular focus is put on the importance of an accurate renormalization of the relevant vertices. We compare with corresponding DSE and lattice results and discuss the apparent convergence of the vertex expansion. Finally, we present numerical evidence for the dynamic mass gap generation in our calculation. Further details, including a thorough discussion of the necessary irregularities, can be found in the appendixes.

II. FRG FLOWS FOR YANG-MILLS THEORY IN A VERTEX EXPANSION

Functional approaches to QCD and Yang-Mills theory are based on the classical gauge fixed action of $SU(3)$ Yang-Mills theory. In general covariant gauges in four dimensions it is given by

$$S_{\mathrm{cl}} = \int_x \frac{1}{4} F^a_{\mu\nu} F^a_{\mu\nu} + \frac{1}{2\xi} \int_x (\partial_\mu A^a_\mu)^2 - \int_x \bar{c}^a \partial_\mu D^{ab}_\mu c^b. \quad (1)$$

Here, ξ denotes the gauge fixing parameter, which is taken to zero in the Landau gauge and $\int_x = \int \mathrm{d}^4 x$. The field strength tensor and covariant derivative are given by

$$\begin{aligned} F^a_{\mu\nu} &= \partial_\mu A^a_\nu - \partial_\nu A^a_\mu + g f^{abc} A^b_\mu A^c_\nu, \\ D^{ab}_\mu &= \delta^{ab} \partial_\mu - g f^{abc} A^c_\mu, \end{aligned} \quad (2)$$

using the fundamental generators T^a, defined by

$$[T^a, T^b] = i f^{abc} T^c, \qquad \mathrm{tr}(T^a T^b) = \frac{1}{2} \delta^{ab}. \quad (3)$$

In general, our notation follows the one used in the works [1,32,33] of the fQCD collaboration [34].

A. Functional renormalization group

We use the functional renormalization group approach as a nonperturbative tool to investigate Yang-Mills theory. The FRG is built on a flow equation for the one-particle irreducible (1PI) effective action or free energy of the theory, the Wetterich equation [35]. It is based on Wilson's idea of introducing an infrared momentum cutoff scale k. Here, this infrared regularization of the gluon and ghost fluctuations is achieved by modifying the action $S_{\mathrm{cl}} \to S_{\mathrm{cl}} + \Delta S_k$ with

$$\Delta S_k = \int_x \frac{1}{2} A^a_\mu R^{ab}_{k,\mu\nu} A^b_\nu + \int_x \bar{c}^a \, R^{ab}_k c^b. \quad (4)$$

The regulator functions R_k are momentum-dependent masses that suppress the corresponding fluctuations below momentum scales $p^2 \approx k^2$ and vanish in the ultraviolet for momenta $p^2 \gg k^2$. See Appendix E for details on the regulators used in the present work. Consequently, the effective action, $\Gamma_k[\phi]$, is infrared regularized, where ϕ denotes the superfield

$$\phi = (A, c, \bar{c}). \quad (5)$$

The fluctuations of the theory are then successively taken into account by integrating the flow equation for the effective action, see e.g. [36,37],

$$\partial_t \Gamma_k[\phi] = \int_p \frac{1}{2} G^{\mu\nu}_{k,ab}[\phi] \partial_t R^{ba}_{k,\mu\nu} - \int_p G^{ab}_k[\phi] \partial_t R^{ba}_k. \quad (6)$$

where $\int_p = \int \mathrm{d}^4 p/(2\pi)^4$. Here we have introduced the RG-time $t = \ln(k/\Lambda)$ with a reference scale Λ, which is typically chosen as the initial UV cutoff Λ. Although this flow equation comes in a simple one-loop form, it provides an exact relation due to the presence of the full field-dependent propagator,

$$G_k[\phi](p,q) = \frac{1}{\Gamma^{(2)}_k[\phi] + R_k}(p,q), \quad (7)$$

on its right-hand side. Furthermore, the flow is infrared and ultraviolet finite by construction. Via the integration of momentum shells in the Wilsonian sense, it connects the ultraviolet, bare action $S_{\mathrm{cl}} = \Gamma_{k\to\Lambda\to\infty}$ with the full quantum effective action $\Gamma = \Gamma_{k\to 0}$.

The flow equations for propagators and vertices are obtained by taking functional derivatives of (6). At the vacuum expectation values, these derivatives give equations for the 1PI correlation functions $\Gamma^{(n)}_k = \delta^n \Gamma_k / \delta\phi^n$, which inherit the one-loop structure of (6). As the cutoff-derivative of the regulator functions, $\partial_t R_k$, decays sufficiently fast for large momenta, the momentum integration in (6) effectively receives only contributions for momenta $p^2 \lesssim k^2$. Furthermore, the flow depends solely on dressed vertices and propagators, leading to a consistent RG and momentum scaling for each diagram resulting from derivatives of (6). Despite its simple structure, the resulting system of equations does not close at a finite number of correlation functions. In general, higher derivatives up to the order $\Gamma^{(n+2)}_k$ of the effective action appear on the right-hand side of the functional relations for the correlation functions $\Gamma^{(n)}_k$.

B. Vertex expansion of the effective action

The structural form of the functional equations discussed in the previous section necessitates the use of approximations in most practical application. One systematic expansion scheme is the vertex expansion, i.e. an expansion of the effective action in terms of 1PI Green's functions. This yields an infinite tower of coupled equations for the correlation functions that has to be truncated at a finite order. This expansion scheme allows a systematic error

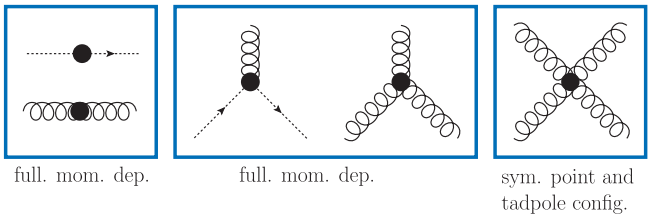

FIG. 1. Approximation for the effective action. Only classical tensor structures are included. See Fig. 2 for diagrams that contribute to the individual propagators and vertices.

estimate in terms of apparent convergence upon increasing the expansion order or improving further approximations for example in the momentum resolution or tensor structures of the included correlation functions. We discuss the convergence of the vertex expansion in Sec. IV B.

Here we calculate the effective action of $SU(3)$ Yang-Mills theory in Landau gauge within a vertex expansion, see Fig. 1 for a pictorial representation. The diagrams contributing to the resulting equations of the constituents of our vertex expansion are summarized graphically in Fig. 2. The lowest order contributions in this expansion are the inverse gluon and ghost propagators parametrized via

$$[\Gamma^{(2)}_{AA}]^{ab}_{\mu\nu}(p) = Z_A(p)p^2\delta^{ab}\Pi^{\perp}_{\mu\nu}(p) + \frac{1}{\xi}\delta^{ab}p_\mu p_\nu,$$
$$[\Gamma^{(2)}_{\bar{c}c}]^{ab}(p) = Z_c(p)p^2\delta^{ab}, \tag{8}$$

with dimensionless scalar dressing functions $1/Z_A$ and $1/Z_c$. Here, $\Pi^{\perp}_{\mu\nu}(p) = \delta_{\mu\nu} - p_\mu p_\nu/p^2$ denotes the corresponding projection operator. We use this splitting in tensor

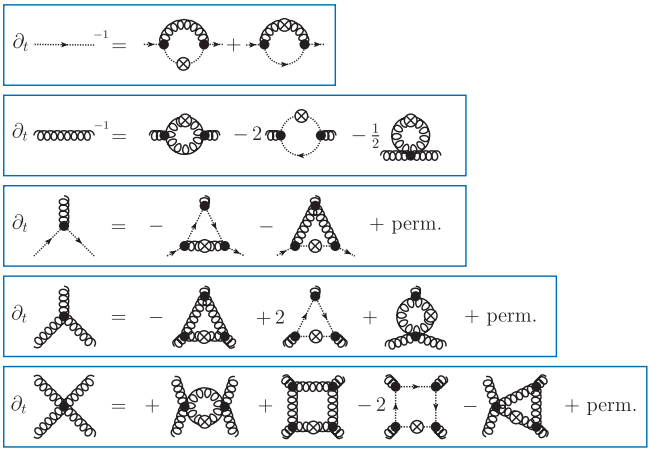

FIG. 2. Diagrams that contribute to the truncated flow of propagators and vertices. Wiggly (dotted) lines correspond to dressed gluon (ghost) propagators, filled circles denote dressed (1PI) vertices and regulator insertions are represented by crossed circles. Distinct permutations include not only (anti-)symmetric permutations of external legs but also permutations of the regulator insertions.

structures with canonical momentum dimension and dimensionless dressings also for the higher order vertices.

On the three-point level we include the full transverse ghost-gluon vertex and the classical tensor structure of the three-gluon vertex

$$[\Gamma^{(3)}_{A\bar{c}c}]^{abc}_{\mu}(p,q) = Z_{A\bar{c}c,\perp}(|p|,|q|,t)[\mathcal{T}_{A\bar{c}c,\mathrm{cl}}]^{abc}_{\mu}(p,q),$$
$$[\Gamma^{(3)}_{A^3}]^{abc}_{\mu\nu\rho}(p,q) = Z_{A^3,\perp}(|p|,|q|,t)[\mathcal{T}_{A^3,\mathrm{cl}}]^{abc}_{\mu\nu\rho}(p,q). \tag{9}$$

Here, the momentum p (q) corresponds to the indices a (b) and t denotes the cosine of the angle between the momenta p and q. The classical tensor structure of the vertices has been summarised as $\mathcal{T}_{A^3,\mathrm{cl}}$ and $\mathcal{T}_{A\bar{c}c,\mathrm{cl}}$, which are listed explicitly in Appendix D. In the case of the transversally projected ghost-gluon vertex, $\mathcal{T}_{A\bar{c}c,\mathrm{cl}}$ represents already a full basis whereas a full basis for the transversally projected three-gluon vertex consists of four elements. However, the effect of nonclassical tensor structures has been found to be subleading in this case [38].

The most important four-point function is given by the four-gluon vertex, which appears already on the classical level. Similarly to the three-gluon vertex, we approximate it with its classical tensor structure

$$[\Gamma^{(4)}_{A^4}]^{abcd}_{\mu\nu\rho\sigma}(p,q,r) = Z_{A^4,\perp}(\bar{p})[\mathcal{T}_{A^4,\mathrm{cl}}]^{abcd}_{\mu\nu\rho\sigma}(p,q,r), \tag{10}$$

see Appendix D for details. The dressing function of the four-gluon vertex is approximated from its momentum dependence at the symmetric point via the average momentum $\bar{p} \equiv \sqrt{p^2+q^2+r^2+(p+q+r)^2}/2$, which has been shown to be a good approximation of the full momentum dependence [39,40]. To improve this approximation further, we additionally calculate the momentum dependence of the four-gluon dressing function $Z_{A^4,\perp}(|p|,|q|,t)$ on the special configuration $(p,q,r) = (p,q,-p)$. We use this special configuration exclusively in the tadpole diagram of the gluon propagator equation, cf. Sec. IV B. We show the difference between the special configuration and the symmetric point approximation in the appendix in Fig. 11. Although the four-gluon vertex has been the subject of several studies [39–43], no fully conclusive statements about the importance of additional nonclassical tensors structures are available.

In summary we have taken into account the propagators and the fully momentum-dependent classical tensor structures of the three-point functions, as well as selected momentum-configurations of the gluon four-point function, see the paragraph above, and Appendix D. For a comparison of the current approximation with that used in other functional works one has to keep in mind that FRG, Dyson-Schwinger or nPI equations implement different resummation schemes. Thus, even on an identical approximation level of a systematic vertex expansion, the included resummations differ.

In the present work we solve the coupled system of all momentum-dependent classical vertex structures and propagators. In former works with functional methods, see e.g. [14–23,38–50], only subsets of these correlation functions have been coupled back. A notable exception is [24], where a similar self-consistent approximation has been used for three-dimensional Yang-Mills theory.

C. Modified Slavnov-Taylor identities and transversality in Landau gauge

In Landau gauge, the dynamical system of correlation functions consists only of the transversally projected correlators [9]. Those with at least one longitudinal gluon leg do not feed back into the dynamics. To make these statements precise, it is useful to split correlation functions into purely transverse components and their complement with at least one longitudinal gluon leg. The purely transverse vertices $\Gamma^{(n)}_{\perp}$, are defined by attaching transverse projection operators to the corresponding gluon legs,

$$[\Gamma^{(n)}_{\perp}]_{\mu_1\cdots\mu_{n_A}} \equiv \Pi^{\perp}_{\mu_1\nu_1}\cdots\Pi^{\perp}_{\mu_{n_A}\nu_{n_A}}[\Gamma^{(n)}]_{\nu_1\cdots\nu_{n_A}}, \tag{11}$$

where n_A is the number of gluon legs and group indices and momentum arguments have been suppressed for the sake of brevity. This defines a unique decomposition of n-point functions into

$$\Gamma^{(n)} = \Gamma^{(n)}_{\perp} + \Gamma^{(n)}_{\mathrm{L}}, \tag{12}$$

where the longitudinal vertices $\Gamma^{(n)}_{\mathrm{L}}$, have at least one longitudinal gluon leg. Consequently, they are always projected to zero by the purely transverse projection operators of (11).

Functional equations for the transverse correlation functions close in the Landau gauge, leading to the structure [9],

$$\Gamma^{(n)}_{\perp} = \mathrm{Diag}[\{\Gamma^{(n)}_{\perp}\}]. \tag{13}$$

In (13) Diag stands for diagrammatic expressions of either integrated FRG, Dyson-Schwinger or nPI equations. Equation (13) follows from the fact that all internal legs are transversally projected by the Landau gauge gluon propagator. Hence, by using transverse projections for the external legs one obtains (13). In contradistinction to this, the functional equations for the vertices with at least one longitudinal gluon leg, $\Gamma^{(n)}_{\mathrm{L}}$, are of the form

$$\Gamma^{(n)}_{\mathrm{L}} = \mathrm{Diag}[\{\Gamma^{(n)}_{\mathrm{L}}\}, \{\Gamma^{(n)}_{\perp}\}]. \tag{14}$$

In other words, the solution of the functional equations (14) for $\Gamma^{(n)}_{\mathrm{L}}$ requires also the solution of the transverse set of equations (13).

In the present setting, gauge invariance is encoded in modified Slavnov-Taylor identities (mSTIs) and Ward-Takahashi identities (mWTIs). They are derived from the standard Slavnov-Taylor identities (STIs) by including the gauge or BRST variations of the regulator terms, see [5,14,51–54] for details. The mSTIs are of the schematic form

$$\Gamma^{(n)}_{\mathrm{L}} = \mathrm{mSTI}[\{\Gamma^{(n)}_{\mathrm{L}}\}, \{\Gamma^{(n)}_{\perp}\}, R_k], \tag{15}$$

which reduce to the standard STIs in the limit of vanishing regulator, $R_k \equiv 0$. The STIs and mSTIs have a similar structure as (14) and can be used to obtain information about the longitudinal part of the correlators. Alternatively, they provide a nontrivial consistency check for approximate solutions of (14).

1. Consequences of the STIs & mSTIs

For the purposes of this work, the most important effect of the modification of the STIs due to the regulator term is that it leads to a nonvanishing gluon mass parameter [51],

$$\Delta_{\mathrm{mSTI}}[\Gamma^{(2)}_{AA}]^{ab}_{\mu\nu} \propto \delta^{ab}\delta_{\mu\nu}\alpha(k)k^2. \tag{16}$$

At $k = 0$, where the regulators vanish, this modification disappears, as the mSTIs reduce to the standard STIs. In particular, this entails that, at $k = 0$, the inverse longitudinal gluon propagator, $\Gamma^{(2)}_{AA,\mathrm{L}}$, reduces to the classical one, solely determined by the gauge fixing term

$$p_\mu([\Gamma^{(2)}_{AA,\mathrm{L}}]^{ab}_{\mu\nu}(p) - [S^{(2)}_{AA,\mathrm{L}}]^{ab}_{\mu\nu}(p)) = 0. \tag{17}$$

This provides a unique condition for determining the value of the gluon mass parameter (16) at the ultraviolet initial scale Λ. However, it can only serve its purpose, if the longitudinal system is additionally solved.

One further conclusion from (15) is that the mSTIs do not constrain the transverse correlation functions without further input. This fact is not in tension with one of the main applications of STIs in perturbation theory, i.e. relating the running of the relevant vertices of Yang-Mills theory that require renormalization. As Yang-Mills theory is renormalizable, only the classical vertex structures are renormalized and hence the renormalization functions of their transverse and longitudinal parts have to be identical.

As an instructive example we consider the ghost-gluon vertex. For this example and the following discussions we evaluate the STIs within the approximation used in the present work: on the right hand side of the STIs we only consider contributions from the primitively divergent vertices. In particular, this excludes contributions from the two-ghost–two-gluon vertex. The ghost-gluon vertex can be parametrized with two tensor structures,

$$[\Gamma^{(3)}_{A\bar{c}c}]^{abc}_{\mu}(p,q) = \mathrm{i} f^{abc}[q_\mu Z_{A\bar{c}c,\mathrm{cl}}(p,q) + p_\mu Z_{A\bar{c}c,\mathrm{ncl}}(p,q)]. \tag{18}$$

In (18) we have introduced two dressing functions $Z_{A\bar{c}c,\mathrm{cl}}$ and $Z_{A\bar{c}c,\mathrm{ncl}}$ as functions of the gluon momentum p and anti-ghost momentum q. In a general covariant gauge only $Z_{A\bar{c}c,\mathrm{cl}}$ requires renormalization. Similar splittings into a classical tensor structure and the rest can be used in other vertices. Trivially, this property relates the perturbative RG-running of the transverse and longitudinal projections of the classical tensor structures. Then, the STIs can be used to determine the perturbative RG-running of the classical tensor structures, leading to the well-known perturbative relations

$$\frac{Z^2_{A\bar{c}c,\mathrm{cl}}}{Z_c^2 Z_A} = \frac{Z^2_{A^3,\mathrm{cl}}}{Z_A^3} = \frac{Z_{A^4,\mathrm{cl}}}{Z_A^2}, \tag{19}$$

at the renormalization scale μ. Consequently, (19) allows for the definition of a unique renormalized two-loop coupling $\alpha_s(\mu)$ from the vertices.

The momentum dependent STIs can also be used to make the relation (19) momentum-dependent. Keeping only the classical tensor structures, we are led to the momentum dependent running couplings

$$\begin{aligned}
\alpha_{A\bar{c}c}(p) &= \frac{1}{4\pi}\frac{Z^2_{A\bar{c}c,\perp}(p)}{Z_A(p)Z_c^2(p)}, \\
\alpha_{A^3}(p) &= \frac{1}{4\pi}\frac{Z^2_{A^3,\perp}(p)}{Z_A^3(p)}, \\
\alpha_{A^4}(p) &= \frac{1}{4\pi}\frac{Z_{A^4,\perp}(p)}{Z_A^2(p)},
\end{aligned} \tag{20}$$

where the used transverse projection is indicated by the subscript $\perp$, for details see Appendix D. Additionally, the vertices appearing in (20) are evaluated at the symmetric point, see Sec. IV B for the precise definition. The STIs and two-loop universality demand that these running couplings become degenerate at large perturbative momentum scales, where the longitudinal and transverse parts of the vertices agree.

In Landau gauge, the ghost-gluon vertex is not renormalized on specific momentum configurations, and we can alternatively define a running coupling from the wave function renormalization of ghost and gluon [15,55],

$$\alpha_s(p) = \frac{1}{4\pi}\frac{g^2}{Z_A(p)Z_c^2(p)}. \tag{21}$$

Note that the momentum-dependence of the running coupling (21) does not coincide with that of the corresponding running couplings obtained from other vertices, i.e. (20). This is best seen in the ratio $\alpha_{A\bar{c}c}(p)/\alpha_s(p) = Z^2_{A\bar{c}c,\perp}(p)/g^2$. In this context we also report on an important result for the quark-gluon vertex coupling,

$$\alpha_{A\bar{q}q}(p) = \frac{1}{4\pi}\frac{Z_{A\bar{q}q,\perp}(p)^2}{Z_A(p)Z_q(p)^2}, \tag{22}$$

with the dressing function of the classical tensor structure of the quark-gluon vertex $Z_{A\bar{q}q,\perp}(p)^2$ and the quark dressing function $1/Z_q(p)$ [1]. The solution of the corresponding STI reveals that the quark-gluon vertex coupling $\alpha_{A\bar{q}q}$ agrees perturbatively with $\alpha_s(p)$ in (21), and hence it differs from the other vertex couplings in (20). Note that the present truncation only considers contributions from primitively divergent vertices. Accordingly, the two-quark–two-ghost vertex contribution in the STI for the quark-gluon vertex, see e.g. [4], has been dropped.

III. CONFINEMENT, GLUON MASS GAP, AND IRREGULARITIES

It has been shown in [37,56–59] that a mass gap in the gluon propagator signals confinement in QCD in covariant gauges. Furthermore, in Yang-Mills theory formulated in covariant gauges, the gapping of the gluon relative to the ghost is necessary and sufficient for producing a confining potential for the corresponding order parameter, the Polyakov loop. Hence, understanding the details of the dynamical generation of a gluon mass gap gives insight into the confinement mechanism.

This relation holds for all potential infrared closures of the perturbative Landau gauge. The standard infrared closure corresponds to a full average over all Gribov regions. This leads to the standard Zinn-Justin equation as used in the literature, e.g. [4]. In turn, the restriction to the first Gribov regime can be implemented within the refined Gribov-Zwanziger formalism, e.g. [60–64], that leads to infrared modifications of the STIs. In the following we discuss the consequences of the standard STIs, a discussion of the refined Gribov-Zwanziger formalism is deferred to future work.

A. Gluon mass gap and irregularities

In order to study the dynamical generation of the mass gap, we first discuss the consequences of the STI for the longitudinal gluon two point function (17). It states that no quantum fluctuations contribute to the inverse longitudinal gluon propagator, i.e. the longitudinal gluon propagator is defined by the gauge fixing term. Therefore, the dynamical creation of a gluon mass gap requires different diagrammatic contributions to the longitudinal and transverse gluon mass parameter. The discussion of the prerequisites for meeting this condition is qualitatively different for the scaling and the decoupling solutions. Hence, these two cases are discussed separately.

The scaling solution is characterized by the infrared behavior [15,18,65–71]

$$\lim_{p\to 0} Z_c(p^2) \propto (p^2)^{\kappa},$$
$$\lim_{p\to 0} Z_A(p^2) \propto (p^2)^{-2\kappa}, \tag{23}$$

with the scaling coefficient $1/2 < \kappa < 1$. A simple calculation presented in Appendix A shows that the ghost loop with an infrared constant ghost-gluon vertex and scaling ghost propagator is already capable of inducing a splitting in the longitudinal and transverse gluon mass parameter.

Next we investigate the decoupling solution, e.g. [21,22], which scales with

$$\lim_{p\to 0} Z_c(p^2) \propto 1,$$
$$\lim_{p\to 0} Z_A(p^2) \propto (p^2)^{-1}, \tag{24}$$

at small momenta. Assuming vertices that are regular in the limit of one vanishing gluon momentum, one finds that all diagrammatic contributions to the longitudinal and transverse gluon mass parameter are identical. For example, if the ghost loop were to yield a nonvanishing contribution to the gluon mass gap, the ghost-gluon vertex would have to be a function of the angle $\theta = \arccos(t)$ between the gluon and antighost momenta p and q,

$$\lim_{|p|\to 0} [\Gamma^{(3)}_{A\bar{c}c}]^{abc}_{\mu}(|p|,|q|,t) = [\Gamma^{(3)}_{A\bar{c}c}]^{abc}_{\mu}(0,|q|,t), \tag{25}$$

even in the limit of vanishing gluon momentum $|p| \to 0$. Since the above limit depends on the angle, the vertex is irregular. See Appendix A for more details on this particular case. Similar conclusions can be drawn for all vertices appearing in the gluon propagator equation. Consequently, if all vertices were regular, no gluon mass gap would be created. In particular, regular vertices would entail the absence of confinement. The necessity of irregularities for the creation of a gluon mass gap was already realized by Cornwall [72].

In the light of these findings it is interesting to investigate the consistency of irregularities with further Slavnov-Taylor identities. Therefore, we consider the Slavnov-Taylor identity of the three-gluon vertex, e.g. [4],

$$\begin{aligned} \mathrm{i} r_\rho [\Gamma^{(3)}_{A^3}]^{abc}_{\mu\nu\rho}(p,q,r) &\\ \propto f^{abc} \frac{1}{Z_c(r^2)} &(\tilde{G}_{\mu\sigma}(p,q) q^2 Z_A(q^2) \Pi^{\perp}_{\sigma\nu}(q) \\ &- \tilde{G}_{\nu\sigma}(q,p) p^2 Z_A(p^2) \Pi^{\perp}_{\sigma\mu}(p)), \end{aligned} \tag{26}$$

where $\tilde{G}_{\mu\nu}$ relates to the ghost-gluon vertex via

$$[\Gamma^{(3)}_{A\bar{c}c}]^{abc}_{\mu}(p,q) = \mathrm{i} g f^{abc} q_\nu \tilde{G}_{\mu\nu}(p,q). \tag{27}$$

For a regular $\tilde{G}_{\mu\nu}$ in the limit $p \to 0$ in (26), the scaling solution leads to a singular contribution of the type

$$\lim_{p\to 0} (p^2)^{1-2\kappa} \tilde{G}_{\nu\sigma}(q,0) \Pi^{\perp}_{\sigma\mu}(p) + \text{regular}, \tag{28}$$

where κ is the scaling coefficient from (23). This is consistent with the expected scaling exponent of the three-gluon vertex in this limit [70]. In the same limit, the decoupling solution leads to a singular contribution of the form

$$\lim_{p\to 0} \tilde{G}_{\nu\sigma}(q,0) \Pi^{\perp}_{\sigma\mu}(p) + \text{regular}. \tag{29}$$

Since the transverse projector $\Pi^{\perp}_{\sigma\mu}(p)$ introduces an angular dependence in the limit $p \to 0$, the STI again demands an irregularity in limit of one vanishing momentum. Note that this is just a statement about the three-gluon vertex projected with one nonzero longitudinal leg r_ρ. Although this momentum configuration does not enter the gluon mass gap directly, crossing symmetry implies the necessary irregularity. In summary, these arguments illustrate that also the three-gluon vertex STI is consistent with the necessity of irregularities for both types of solutions.

We close the discussion of vertex irregularities with the remark that the infrared modification of the propagator-STI in the refined Gribov-Zwanziger formalism may remove the necessity for irregularities in the vertices.

B. Origin of irregularities

As discussed in the previous section, self-consistency in terms of the Slavnov-Taylor identities entails a correspondence between the dynamical generation of a gluon mass gap and the presence of irregularities. But the STIs do not provide a mechanism for the creation of irregularities, the gluon mass gap, and in turn confinement.

In the scaling solution, (23), the irregularities arise naturally from the nontrivial scaling. Hence they are tightly linked to the original Kugo-Ojima confinement scenario [73], that requires the nontrivial scaling. Note, however, that this simply links different signatures of confinement but does not reveal the mechanism at work.

For the decoupling solution (24), we want to discuss two possible scenarios. In the first scenario, the irregularities are generated in the far infrared. A second possibility is that they are triggered via a condensate and/or a resonance, providing a direct connection of confinement and spontaneous symmetry breaking.

In the first scenario it is sufficient to focus on ghost loops as possible sources of such irregularities, since the gluonic diagrams decouple from the infrared dynamics due to the gluon mass gap. This is a seemingly appealing scenario as it

is the dynamical ghost that distinguishes confining Yang-Mills theory from e.g. QED. However, in the decoupling solution (24) both, the ghost-gluon vertex as well as the ghost propagator, have infrared finite quantum corrections: no ghost-loops contribute to their equation and (infrared) constant dressing functions can be assumed for both. As a consequence the ghost loop contributions to correlation functions have the same infrared structure as perturbative ghost-loop contributions. However, none of these perturbative ghost loops yields the necessary irregularities, see Appendix B for an explicit calculation.

In the second scenario, the generation of irregularities can be based on the dynamical generation of a nonvanishing transverse background, $F^a_{\mu\nu}F^a_{\mu\nu} \neq 0$, in the infrared. This gluon condensate is the Savvidi vacuum [74], and its generation in the present approach has been discussed in [75] with $F^a_{\mu\nu}F^a_{\mu\nu} \approx 1\ \mathrm{GeV}^4$. Then, a vertex expansion about this nontrivial IR-solution of the equation of motion introduces an IR-splitting of transverse and longitudinal vertices due to the transversality of the background field. This IR-splitting automatically implies irregularities as discussed in Sec. III A, and is sufficient for creating a physical mass gap in the gluon. This scenario provides a direct relation of confinement and spontaneous symmetry breaking. Therefore it is possibly connected to the presence of resonances that are triggered in the longitudinal sector of the theory, where they do not spoil the gapping of the completely transverse sector. A purely longitudinal massless mode, as a source for irregularities in the gluonic vertices, has been worked out in [76,77], for a short summary see [78]. As a consequence, an irregularity appears in the purely longitudinal three-gluon vertex in a way that preserves the corresponding Slavnov-Taylor identity. The creation of a purely transverse background and the presence of longitudinal massless mode would then be two sides of the same coin. Furthermore, the longitudinal resonance has to occur at about the same scale as the gluon condensate, in order to trigger the correct gluon mass gap. A more detailed discussion and computation of this scenario cannot be assessed in the purely transverse system and is therefore deferred to future work.

C. The purely transverse system

In this work we restrict ourselves to a solution of the purely transverse system (13), which is closed. The only relevant UV parameters in this system are the strong coupling and the transverse gluon mass parameter. In the UV the transverse mass parameter agrees with the longitudinal one. The latter is fixed by the mSTI for the longitudinal gluon propagator. Hence, the only information needed from the longitudinal system is the initial value for the transverse gluon mass parameter (16). Note also that there is at least one value for the initial gluon mass parameter that yields a valid confining solution. In the following we vary the gluon mass parameter and discuss the properties of the ensuing solutions. We find a confining branch with both scaling and decoupling solutions. In addition, we observe a transition to the deconfined Higgs-type branch. No Coloumb branch is found. The unique scaling solution satisfies the original Kugo-Ojima confinement criterion with $Z_C(p=0)=0$. We emphasise that the existence of the scaling solution is dynamically generated in a highly nontrivial way. The details are discussed in Sec. IV D.

IV. NUMERICAL RESULTS

We calculate Yang-Mills correlation functions by integrating the self-consistent system of flow equations obtained from functional derivatives of (6), see Fig. 2 for diagrammatic representations. Technical details on the numerical procedure are given in Appendix C. We use constant dressing functions as initial values for the 1PI correlators at the ultraviolet initial scale Λ. Consequently, the initial action Γ_Λ is given by the bare action of QCD and the Slavnov-Taylor identities enforce relations between these constant initial correlation functions. As is well-known, and also discussed in Sec. II C, the Landau gauge STIs leave only three of the renormalization constants independent, namely the value of the strong running coupling and two trivial renormalizations of the fields that drop out of any observable. To eliminate cutoff effects, we choose the constant initial values for the vertex dressings such that the momentum-dependent running couplings, (20) are degenerate at perturbative momentum scales p with $\Lambda_{\mathrm{QCD}} \ll p \ll \Lambda$ i.e. the STIs (19) are only fulfilled on scales considerably below the UV cutoff scale. The modification of the Slavnov-Taylor identity, caused by the regulator term, requires a nonphysical gluonic mass term m^2_Λ at the cutoff Λ. The initial value for the inverse gluon propagator is therefore taken as

$$[\Gamma^{(2)}_{AA,\Lambda}]^{ab}_{\mu\nu}(p) = (Z_{A,\Lambda}p^2 + m^2_\Lambda)\delta^{ab}\Pi^{\perp}_{\mu\nu}(p). \quad (30)$$

The nonphysical contribution m^2_k to the gluon propagator vanishes only as the renormalization group scale, k, is lowered to zero, where the mSTIs reduce to the usual Slavnov-Taylor identities. The initial value m^2_Λ can be uniquely fixed by demanding that the resulting propagators and vertices are of the scaling type. Consequently, the only parameter in this calculation is the value of the strong running coupling at the renormalization scale, as initially stated. We also produce decoupling solutions by varying the gluon mass parameter toward slightly larger values. Our reasoning for their validity as confining solutions is presented in Sec. IV D.

A. Correlation functions and running couplings

We show our results for the Yang-Mills correlation functions as well as the momentum-dependent transverse

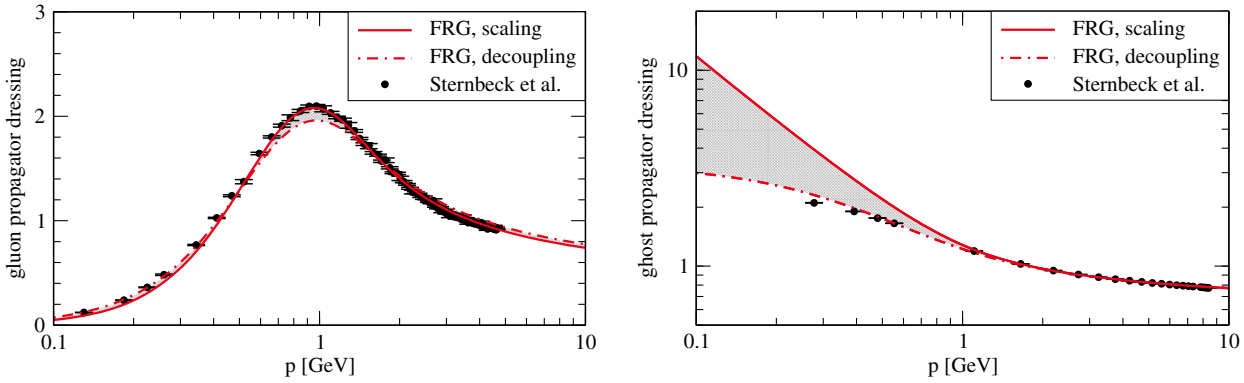

FIG. 3. Gluon dressing $1/Z_A$ (left) and ghost dressing $1/Z_c$ (right) in comparison to the lattice results from [79]. The scale setting and normalisation procedures are described in Appendix F.

running couplings in Figs. 3–6, see also Figs. 11–13 in the appendixes for a comparison of the vertices to recent lattice and DSE results. A discussion of truncation effects is deferred to Sec. IV B. In order to be able to compare to results from lattice simulations, we set the scale and normalize the dressings as described in Appendix F. At all momenta, where the difference between the scaling (solid line) and decoupling (band bounded by dashed-dot line) solutions is negligible, our results for the correlations functions agree very well with the corresponding lattice results. In the case of the scaling solution we find the consistent scaling exponents

$$\begin{aligned}\kappa_{\text{ghost}} &= 0.579 \pm 0.005,\\ \kappa_{\text{gluon}} &= 0.573 \pm 0.002,\end{aligned} \tag{31}$$

where the uncertainties stem from a least square fit with the ansatz

$$\begin{aligned}Z_c(p) &\propto (p^2)^{\kappa_{\text{ghost}}},\\ Z_A(p) &\propto (p^2)^{-2\kappa_{\text{gluon}}}.\end{aligned} \tag{32}$$

As discussed in Sec. III C, the scaling solution is a self-consistent solution of the purely transverse system in the used approach, and has no systematic error related to the lack of solving the longitudinal system. In turn, the presented decoupling solutions suffer from the missing solution of the longitudinal system, leading to a small additional systematic error. This argument already suggests that it is the presented scaling solution that should agree best with the lattice results in the regime $p \gtrsim 1$ GeV, where the solutions show no sensitivity to the Gribov problem. This is confirmed by the results, see in particular Fig. 3.

In the infrared regime, $p \lesssim 1$ GeV, the different solutions approach their infrared asymptotics. In Fig. 3 and Fig. 4 we compare the FRG solutions with the lattice data from [79]. In agreement with other lattice results [80–82] in four dimensions, these propagators show a decoupling behavior, for a review see [12]. Taking the IR behavior of all correlators into account, cf. also Fig. 13, the lattice solution [79] is very close to the decoupling solution (dot-dashed line) that is furthest from the scaling solution (solid line). Note however, that the systematic errors of both approaches, FRG computations and lattice simulations increase toward the IR. While the FRG computations lack apparent convergence in this regime, the lattice data are affected by the nonperturbative gauge fixing procedure, i.e. the choice of Gribov copies [83–85] and discretization artefacts [86]. Consequently, comparing the FRG IR band

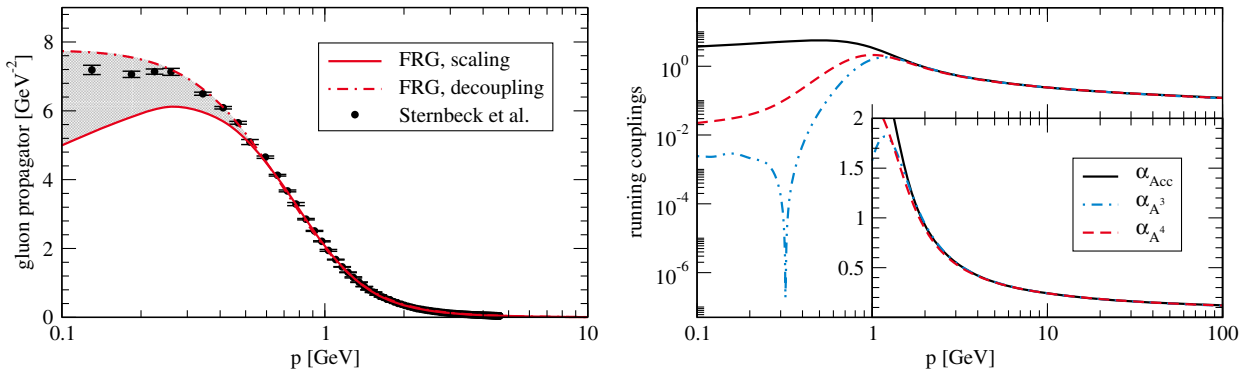

FIG. 4. Left: Gluon propagator in comparison to the lattice results from [79]. Right: Effective running couplings defined in (20) as obtained from different Yang-Mills vertices as function of the momentum.

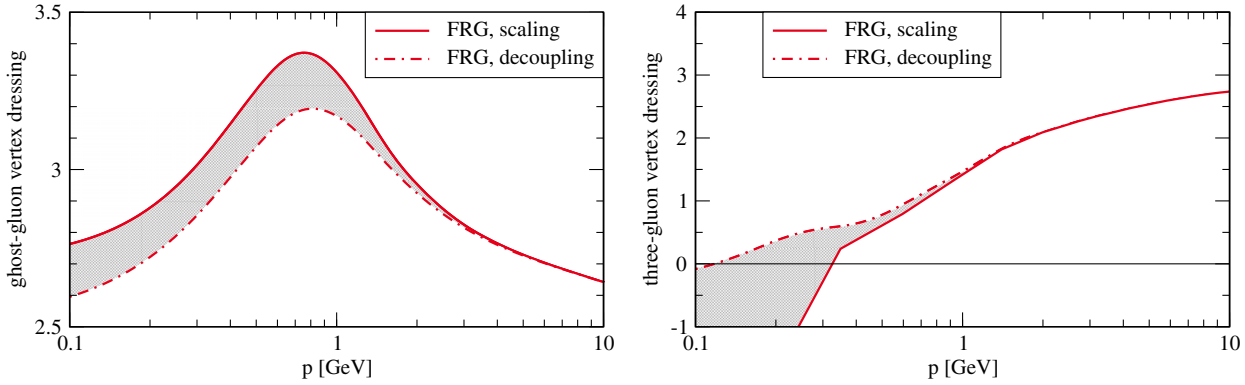

FIG. 5. Ghost-gluon vertex (left) and three-gluon (right) vertex dressing functions $Z_{A\bar{c}c,\perp}(p,p,-\frac{1}{2})$ and $Z_{A^3,\perp}(p,p,-\frac{1}{2})$ in the symmetric point configuration. More momentum configurations and comparisons to Dyson-Schwinger and lattice results can be found in Figs. 11–13. In contrast to Fig. 3, the decoupling dressings are normalised to the scaling solution in the UV.

to the lattice propagators has to be taken with a grain of salt. In the case of the vertices, we compare also to results obtained within the Dyson-Schwinger equation approach [39,44,47], see Fig. 7 and 13. A comparison of the different running vertex couplings is given in Sec. IV C.

We find that it is crucial to ensure the degeneracy in the different running vertex couplings at perturbative momentum scales in order to achieve quantitative accuracy, see also Sec. IV B. The transverse effective running couplings, as defined in (20), are shown in the right panel of Fig. 4. To be able to cover a larger range of momenta with manageable numerical effort, the shown running couplings have been obtained within an approximation that takes only one momentum variable into account in the vertices, see Sec. IV B. At large perturbative momentum scales, we find them to be perfectly degenerate, as is demanded by the Slavnov-Taylor identities. The degeneracy of the running couplings is lifted at a scale of roughly 2 GeV, which coincides with the gapping scale of the gluon. Furthermore, the three-gluon vertex shows a zero crossing at scales of 0.1 GeV to 0.33 GeV, which is the reason for the spike in the corresponding running coupling. This zero crossing, which is caused by the infrared-dominant ghost-loop, is well-known in the literature [38,46,47,87]. Even though we are looking at the scaling solution, we find that the running couplings defined from the purely gluonic vertices are still strongly suppressed in the infrared. In particular the three-gluon vertex running coupling becomes more strongly suppressed than the four-gluon vertex running coupling. However, as demanded by scaling, they seem to settle at tiny but finite fixed point values, which has also been seen in Dyson-Schwinger studies [38,39,41].

B. Quality of the approximation

In Fig. 6 (right panel), we show the scaling solution for the propagators in different truncations. In all cases, the full momentum dependence of the propagators is taken into account whereas different approximations are used for the vertices. Including only RG-scale-dependent constant vertex dressing functions is the minimal approximation that can produce a scaling solution with a physical gluon mass gap. The dot-dashed (magenta) line in Fig. 6 (right panel) corresponds to an approximation with constant vertex dressing functions evaluated at the symmetric configuration

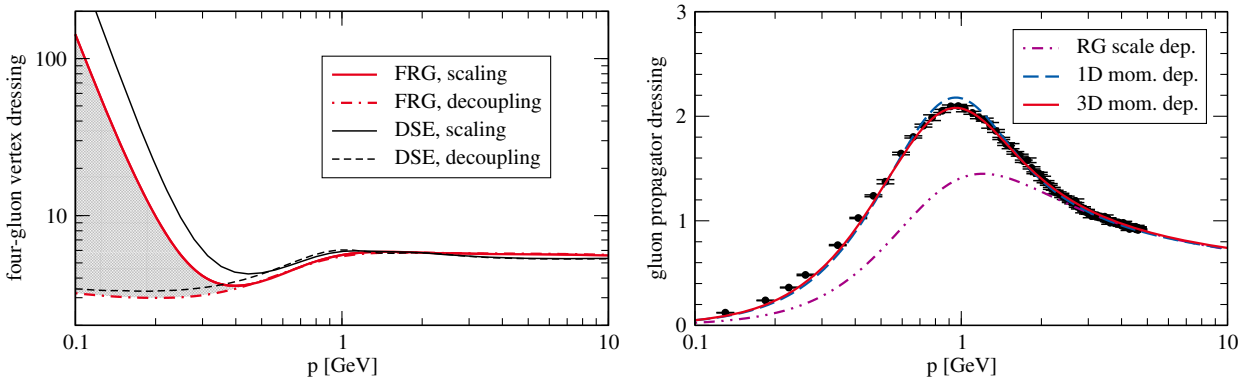

FIG. 6. Left: Four-gluon vertex dressing function as defined in (10) at the symmetric point in comparison to Dyson-Schwinger computations [39]. We normalized all curves to match the scaling result at $p = 2$ GeV. Right: Gluon propagator dressings obtained with different momentum approximations, see Sec. IV B for details.

with momentum $\mathcal{O}(250\ \mathrm{MeV})$. Hence the vertices are only RG-scale-dependent vertices. For the dashed blue results the dressing functions for the transversally projected classical tensor structures have been approximated with a single momentum variable $\bar{p}^2 \equiv \frac{1}{n}\sum_{i=1}^{n} p_i^2$. Reducing the momentum dependence to a single variable requires the definition of a momentum configuration to evaluate the flow. Here, we use the symmetric point configuration, defined by $p_i \cdot p_i = p^2$ and $p_i \cdot p_j = -1/(n-1)$ for $i \neq j$, where $n = 3(4)$ for the three(four)-gluon vertex. Finally, the solid red line corresponds to our best truncation. As described in Sec. II B, it takes into account the full momentum dependence of the classical tensors structures of the three-point functions as well as the four-gluon vertex in a symmetric point approximation. Additionally, all (three-dimensional) momentum configurations of the four-gluon vertex that are needed in the tadpole diagram of the gluon propagator equation have been calculated and coupled back in this diagram. The reliability of our approximation can be assessed by comparing the two simpler truncations to the result obtained in our best truncation scheme. We observe that our results apparently converge toward the lattice result, as we improve the momentum approximation for the vertices.

The effects of nonclassical tensor structures and vertices are beyond the scope of the current work and have to be checked in future investigations, see however [38] for an investigation of nonclassical tensor structures of the three-gluon vertex. Within the present work, the already very good agreement with lattice results suggests, that their influence on the propagators is small.

The final gluon propagator is sensitive to the correct renormalization of the vertices. For example, a one percent change of the three-gluon vertex dressing at an UV scale of 20 GeV magnifies by up to a factor 10 in the final gluon propagator. Therefore, small errors in the perturbative running of the vertices propagate, via renormalization, into the two-point functions. We expect a five percent uncertainty in our results due to this.

Despite these uncertainties, we interpret the behavior in Fig. 6 (right panel) as an indication for apparent convergence.

C. Comparison to other results

In Fig. 13, numerical results for the ghost-gluon and three-gluon vertices are shown in comparison to other functional methods as well as lattice results. In summary, the results from various functional approaches and the lattice agree to a good degree. But these correlation functions are not renormalization group invariant, and a fully meaningful comparison can only be made with RG invariant quantities. Therefore, we compare our results for the RG invariant running couplings with the respective results from DSE computations. To be more precise, it is actually the β functions of the different vertices that are tied together by two-loop universality in the sense that they should agree in the regime where three-loop effects are negligible. Since constant factors drop out of the β functions, we have normalized the DSE running couplings to the FRG result at large momentum scales in Fig. 7. For the sake of visibility, we only have provided a band for the spread of the FRG couplings as obtained from different vertices. The shown DSE running couplings are based on a series of works [39,44,47,50,88], where the explicitly shown results are taken from [39,47,89,90]. Additionally, we provide the raw DSE running couplings that have not been rescaled by a constant factor in the inlay.

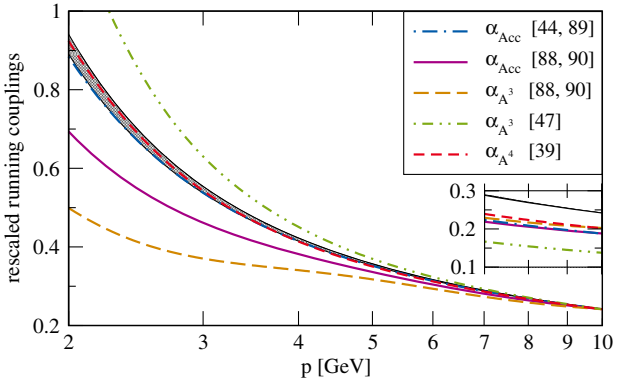

FIG. 7. Running couplings (20) in comparison with DSE running. The grey band gives the spread of vertex couplings from the FRG in the present work. The DSE results are shown rescaled to fit our ghost-gluon vertex running coupling at 10 GeV to facilitate the comparison. The inlay shows the unscaled couplings. Note that the FRG running couplings naturally lie on top of each other and are not depicted rescaled.

D. Mass gap, mSTIs and types of solutions

As discussed in Sec. II C, the introduction of the regulator in the FRG leads to a modification of the Slavnov-Taylor identities. In turn the inverse gluon propagator obtains a contribution proportional to $\Delta\Gamma^{(2)}_{AA} \propto k^2\alpha(k)$ for all $k > 0$. Disentangling the physical mass gap contribution from this mSTI contribution to the gluon mass parameter is intricate, both conceptually and numerically. The resulting numerical challenge is illustrated in the appendix in Fig. 10, where we show the k-running of the gluon mass parameter. This is the analogue of the problem of quadratic divergences in Dyson-Schwinger equations with a hard momentum cutoff, see e.g. [91]. However, there has to exist at least one choice for the gluon mass parameter m_Λ^2 that yields a valid confining solution, see Sec. II C. To resolve the issue of finding this value, we first recall that a fully regular solution has no confinement and necessarily shows a Higgs- or Coulomb-type behavior. Although we do not expect these branches to be consistent solutions, we can trigger them by an appropriate choice of the gluon mass parameter in the UV. The confinement branch then lies between the Coulomb and the Higgs

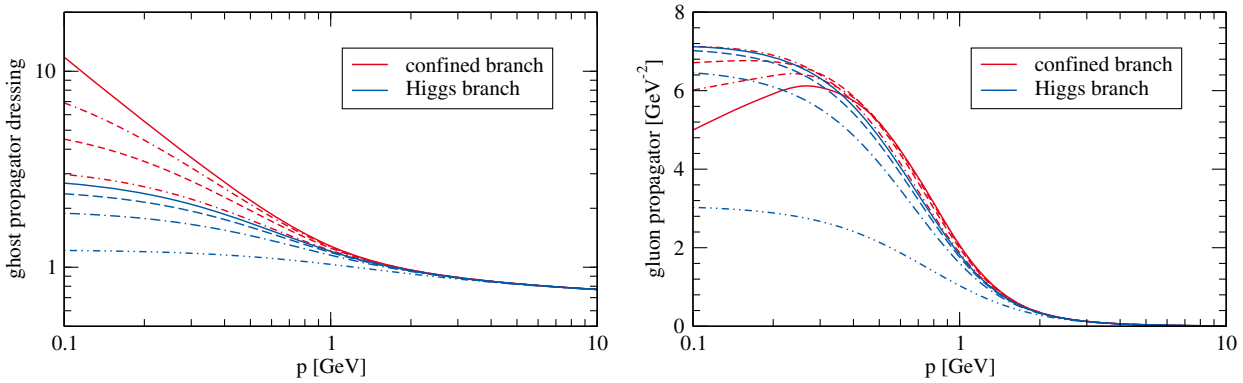

FIG. 8. Ghost dressing functions $1/Z_c$ (left) and gluon propagators (right) for different values of the ultraviolet gluon mass parameter. Blue results correspond to the Higgs-type branch and red results to the confined branch. The solutions in all branches have been normalized to the scaling solution in the UV.

branch. We need, however, a criterion for distinguishing between the confinement and the Higgs-type branch.

To investigate the possible solutions in a controlled way, we start deep in the Higgs-type branch: an asymptotically large initial gluon mass parameter m^2_Λ triggers an explicit mass term of the gluon at $k = 0$. If we could trigger this consistently in the present $SU(3)$ theory, it would constitute a Higgs solution. Note that in the current approximation it cannot be distinguished from massive Yang-Mills theory, which has e.g. been considered in [23,92]. Starting from this Higgs-type branch, we can then explore the limit of smaller initial mass parameters. This finally leads us to the scaling solution, which forms the boundary toward an unphysical region characterized by Landau-pole-like singularities. It is left to distinguish between the remaining confining and Higgs-type solutions, shown in Fig. 8, without any information from the longitudinal set of equations. For that purpose we use two criteria:

In the left panel of Fig. 9, we show the mass gap of the gluon, $m^2 = \Gamma^{(2)}_{AA,k=0}(p = 0)$, as a function of the chosen initial value for the gluon mass parameter m^2_Λ subtracted by the corresponding value for the scaling solution $m^2_{\Lambda,\text{scaling}}$. The latter solution corresponds to zero on the x-axis in Fig. 9. As mentioned before, going beyond the scaling solution, $m^2_\Lambda < m^2_{\Lambda,\text{scaling}}$, leads to singularities. We interpret their presence as a signal for the invalidity of the Coulomb branch as a possibly realization of non-Abelian Yang-Mills theory. The decisive feature of the left panel of Fig. 9 is the presence of a minimum at m^2_{min}. If there were no dynamical mass gap generation, m^2 would have to go to zero as we lower m^2_Λ. In contrast to this, we find that the resulting gluon mass gap is always larger than the value it takes at $m^2_\Lambda = m^2_{\text{min}}$. In particular, this entails that all solutions to the left of the minimal value, $m^2_\Lambda < m^2_{\text{min}}$, are characterized by a

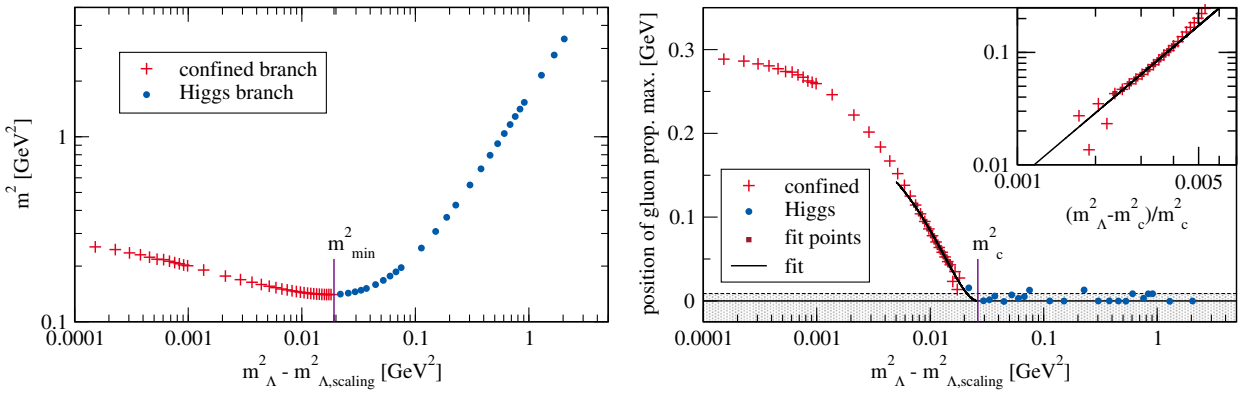

FIG. 9. Left: Gluon mass gap as a function of the gluon mass parameter $m^2_\Lambda - m^2_{\Lambda,\text{scaling}}$, where $m^2_{\Lambda,\text{scaling}}$ denotes the gluon mass parameter that yields the scaling solution. Right: Momentum value at which the gluon propagator assumes its maximum, as a function of the gluon mass parameter $m^2_\Lambda - m^2_{\Lambda,\text{scaling}}$. The inlay exposes the power law behavior of the gluon propagator maximum in the vicinity of the transition region, see (33). Both plots were obtained from our numerically less-demanding 1D approximation. We have repeated this analysis in the transition regime from Higgs-type to confinement branch also with the best approximation and find the same behavior. The shaded area marks momentum scales that are not numerically resolved in the present work. The points in this region rely on a generic extrapolation.

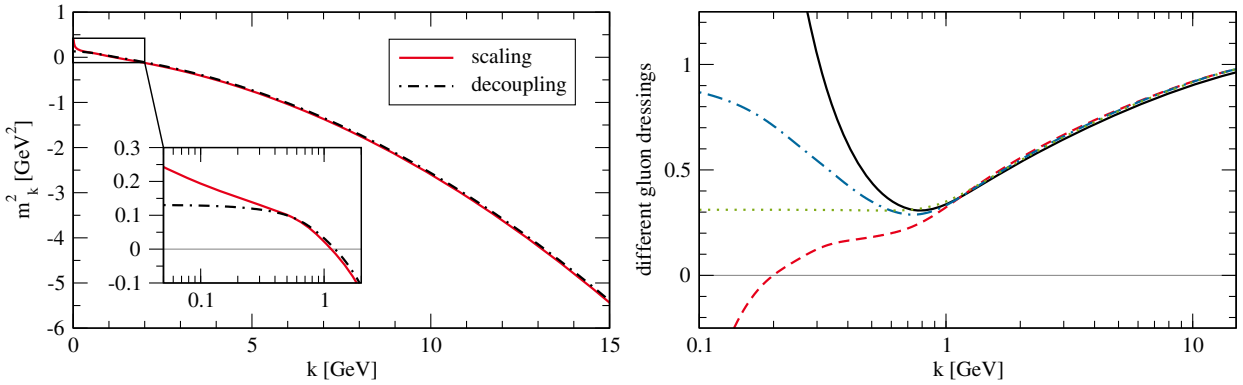

FIG. 10. Left: Gluon mass parameter $m_k^2 = \Gamma^{(2)}_{AA,k}(p=0)$ over k. Right: Possible choices for the scaling prefactor in the gluon regulator: $Z_{A,k}(k)$ (black, solid), $\bar{Z}_{A,k}(k)$ (red, dashed), $\hat{Z}_{A,k}(k)$ (blue, dot-dashed) and $\tilde{Z}_{A,k}$ (green, dotted) as defined in (E3) and (E5). Independence of the results from the above choice has been checked explicitly.

large dynamical contribution to the gluon mass gap, which we interpret as confinement.

As a second criterion for differentiating between confining and Higgs solutions, we use the presence of a maximum at nonvanishing momenta in the gluon propagator, which signals positivity violation [4]. In the right panel of Fig. 9, we show the location of the maximum in the gluon propagator, again as a function of the gluon mass parameter, $m_\Lambda^2 - m_{\Lambda,\text{scaling}}^2$. We clearly see a region of confining solutions that show a back-bending of the gluon propagator at small momenta, see Fig. 8. The dashed line, separating the shaded from the white region in the right panel of Fig. 9, indicates the smallest momentum value at which the gluon propagator has been calculated. With this restriction in mind, the fit in the inlay demonstrates that the location of the maximum of the propagator scales to zero as one approaches the critical value m_c^2. We fit with

$$p_{\max}(m_\Lambda^2) \propto \left(\frac{m_\Lambda^2 - m_c^2}{m_c^2}\right)^\alpha, \tag{33}$$

which yields the critical exponent

$$\alpha = 1.95 \pm 0.6, \tag{34}$$

in the 1D approximation. Within the numerical accuracy, this boundary value m_c^2 is equivalent to the minimal value m_{min}^2 of our first confinement criterion. Hence, the value of the UV mass parameter that results in the minimal gluon mass gap, is also the one that shows minimal back-bending. Note that the lattice simulations show a gluon propagator that is at least very close to this minimal mass gap.

As discussed in detail in Sec. III and Appendixes A and B, a gluon mass gap necessitates irregularities. The scaling solution by definition contains these irregularities already in the propagators, cf. (23). For the decoupling-type solutions, we excluded infrared irregularities of diagrammatic origin, see Appendix B. Thus, for the decoupling-type solutions our arguments for the validity of the solutions are weaker and remain to be investigated in a solution including at least parts of the longitudinal system, see the discussion in Sec. III. Additionally, it might be necessary to expand about the solution of the equation of motion, see [75].

We summarize the findings of the present section. In the right panel of Fig. 9 we can distinguish a confining branch with positivity violation and a Higgs-type branch with a massive gluon propagator. A Coulomb-type solution, on the other hand, can never be produced with the functional renormalization group since any attempt to do so leads to Landau-pole-like singularities. The nonexistence of the Coulomb branch is tightly linked to the nonmonotonous dependence of the mass gap on the initial gluon mass parameter, see left panel of Fig. 9. This behavior is of a dynamical origin that is also responsible for the existence of the scaling solution for the smallest possible UV gluon mass parameter.

E. Discussion

As has been discussed already in Sec. IV A, one nontrivial feature of the different vertex couplings is their quantitative equivalence for momenta down to $p \approx 2$ GeV, see Fig. 4 (right panel). This property extends the universal running of the couplings into the semiperturbative regime. On the other hand, the couplings violate universality in the nonperturbative regime for $p \lesssim 2$ GeV. The universality down to the semiperturbative regime is a very welcome feature of Landau gauge QCD, as it reduces the size of the nonperturbative regime and hence the potential systematic errors. In particular, one running coupling is sufficient to describe Landau gauge Yang-Mills theory down to momentum scales of the order of the gluon mass gap. This suggests to use the propagators together with the ghost-gluon vertex for simple semiquantitative calculations. The above structure also explains and supports the semiquantitative nature of the results in low-order approximations.

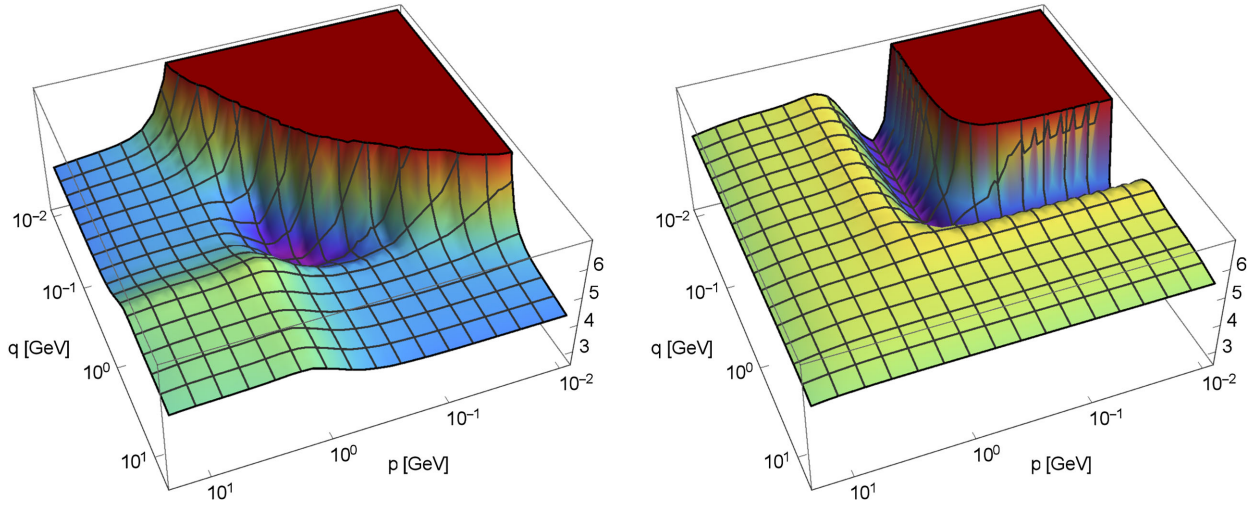

FIG. 11. Left: Four-gluon vertex dressing function $Z_{A^4,\perp}(p,q,0)$ in the tadpole configuration. The angular dependence is small compared to the momentum dependence. Right: Four-gluon tadpole configuration evaluated in the symmetric point approximation, showing a quantitative and qualitative deviation from the full calculation.

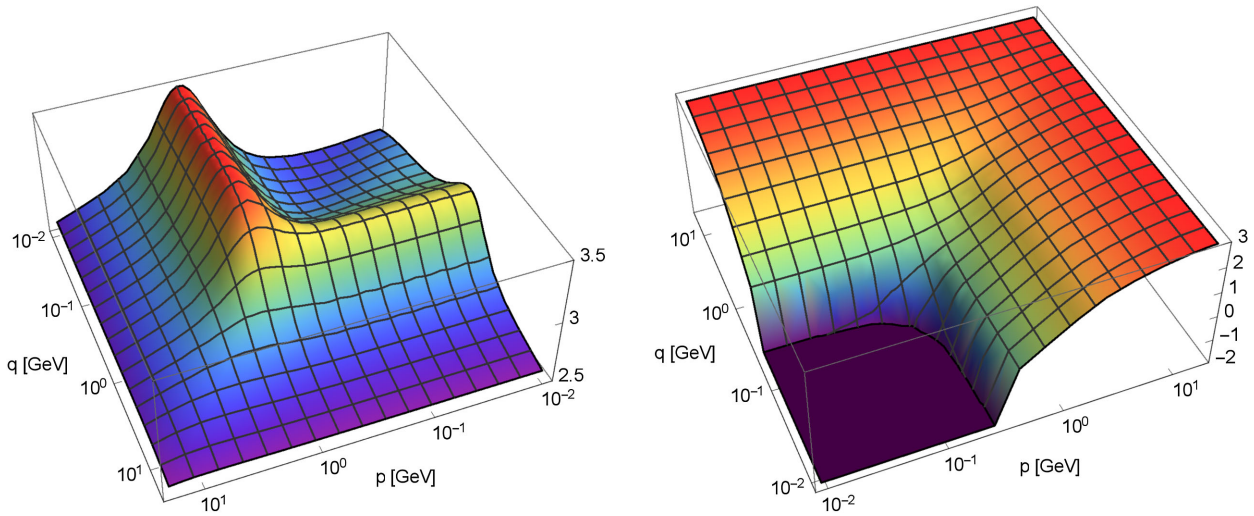

FIG. 12. Left: Ghost-gluon vertex dressing function $Z_{A\bar{c}c,\perp}(p,q,0)$. Right: Three-gluon vertex dressing function $Z_{A^3,\perp}(p,q,0)$.

This implies that self-consistent calculations of most or all vertices have to reproduce this universality, in particular for momenta 2 GeV $\lesssim p \lesssim$ 10 GeV. When starting from the value of the strong running coupling at perturbative momenta, we find that a violation of the degeneracy of the running couplings, (20), in this regime goes hand in hand with the loss of even qualitative properties of the nonperturbative results in self-consistent approximations. This surprising sensitivity to even small deviations of the couplings from their universal running extends to the fully dynamical system with quarks, see e.g. [1,98]. Note in this context that the quark-gluon coupling $\alpha_{A\bar{q}q}$, (22), agrees with the ghost-gluon coupling α_s defined in (21), and not the vertex coupling $\alpha_{A\bar{c}c}$, see Sec. II C. It can be shown in the full QCD system, that deviations from universality on the percent level have a qualitative impact on chiral symmetry breaking. The origin of this is the sensitivity of chiral symmetry breaking to the correct adjustment of physical scales, i.e. $\Lambda_{\rm QCD}$, in all subsystems. These observations underline the relevance of the present results for the quantitative grip on chiral symmetry breaking. A full analysis will be presented in a forthcoming work, [98].

We close this discussion with the remark that universality in the semiperturbative regime is tightly linked with the consistent renormalization of all primitively divergent correlation functions. We find it crucial to demand the validity of the STIs (19) only on momentum scales considerably below the ultraviolet cutoff Λ. On the other hand, the relations (19) are violated close to the ultraviolet cutoff, due to the Bogliubov-Parasiuk-Hepp-Zimmermann

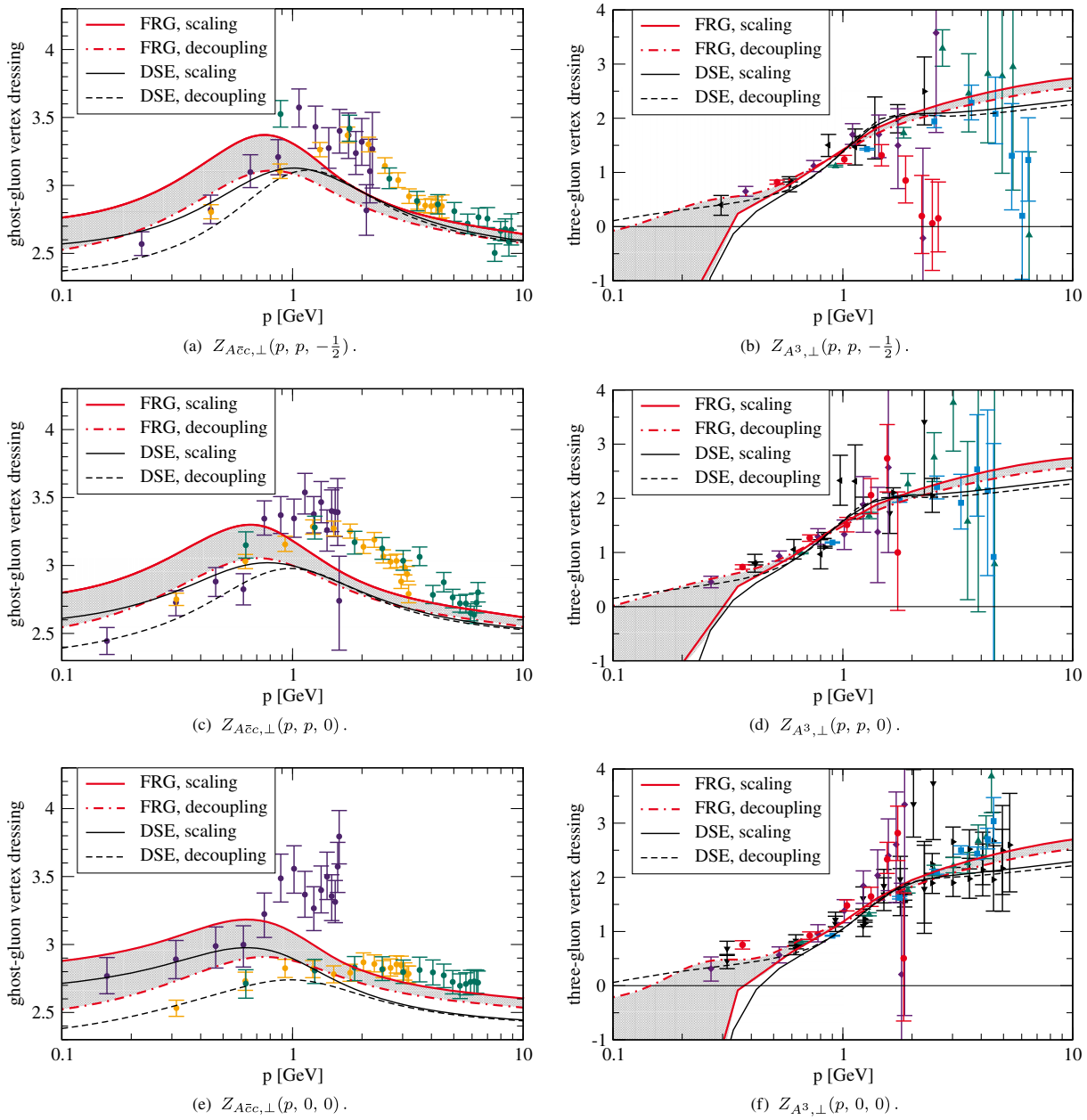

FIG. 13. Left: Ghost-gluon vertex dressing function $Z_{A\bar{c}c,\perp}(p,q,\cos\sphericalangle(p,q))$ in comparison to $SU(2)$ lattice [93–95] and DSE results [44,89]. The lattice results are obtained from $N=32^4$ lattices. The magenta/orange/green points (color online) correspond to $\beta\in\{2.13,2.39,2.60\}$ and lattice spacing $a^{-1}\in\{0.8\text{ GeV},1.6\text{ GeV},3.2\text{ GeV}\}$, respectively. Right: Three-gluon vertex dressing function $Z_{A^3,\perp}(p,q,\cos\sphericalangle(p,q))$ compared with $SU(2)$ lattice [93–95] and Dyson-Schwinger [47] results. The colored lattice points are taken from [93,94] and correspond to $\beta\in\{2.2,2.5\}$ and different lattice sizes $1.4\text{ fm}<L<4.7\text{ fm}$. The lattice results shown in black are based on [93,94] but stem from [95]. These are gained from $N\in\{24^4,32^4\}$ lattices with $\beta\in\{2.13,2.39,2.60\}$ and lattice spacing $a^{-1}\in\{0.8\text{ GeV},1.6\text{ GeV},3.2\text{ GeV}\}$. The comparison with $SU(2)$ lattice simulations is justified since the propagators of $SU(2)$ and $SU(3)$ Yang-Mills theory agree well for a large range of momenta [96,97] after a respective normalization in this regime. We rescaled all DSE results such that they match the scaling solution in the symmetric point configuration at $p=2$ GeV. Note that the scaling and decoupling solutions differ in the UV just due to the different field renormalizations, cf. Fig. 3. The physically relevant couplings, given by (20), agree in the UV.

(BPHZ)-type subtraction schemes. This constitutes no restriction to any practical applications, since the cutoff can always be chosen large enough, such that no violations effects can be found at momenta $p\ll\Lambda$. One particular consequence of BPHZ-type subtraction schemes is then that the calculated renormalization constants necessarily have to violate (19), since they contain contributions from momentum regions close to the ultraviolet cutoff.

V. CONCLUSION

In this work we investigate correlation functions in Landau gauge $SU(3)$ Yang-Mills theory. This analysis is performed in a vertex expansion scheme for the effective action within the functional renormalization group approach. Besides the gluon and ghost propagators, our approximation for the effective action includes the self-consistent calculation of momentum-dependent dressings of the transverse ghost-gluon, three-gluon and four-gluon vertices. Starting from the gauge fixed tree-level perturbative action of Yang-Mills theory, we obtain results for the correlators that are in very good agreement with corresponding lattice QCD simulations. Furthermore, the comparison of different vertex truncations indicates the apparent convergence of the expansion scheme.

Special emphasis is put on the analysis of the dynamical creation of the gluon mass gap at nonperturbative momenta. Self-consistency in terms of the Slavnov-Taylor identities directly links this property to the requirement of IR irregularities in the correlation functions. The source of these irregularities is easily traced back to the IR-divergent ghost propagator for the scaling solution. In the decoupling-type solutions, the source of these irregularities is harder to identify, where the creation of diagrammatic infrared irregularities is ruled out by general arguments. Within our truncation, we can exclude irregularities of nondiagrammatic origin in the purely transverse subsystem. Hence it is necessary to solve the longitudinal system to answer whether the required irregularities are generated for decoupling-type solutions, which is not done in this work. Nevertheless, we are able to produce decoupling-type solutions by invoking two consistent criteria, which allow for the differentiation between confining and Higgs-like solutions. The decoupling-type solutions are bound by the solution that shows the minimal mass gap, which is also the solution with minimal back-bending of the gluon propagator.

ACKNOWLEDGMENTS

We thank Markus Q. Huber, Axel Maas, Fabian Rennecke, Andre Sternbeck and Richard Williams for discussions as well as providing unpublished data. This work is supported by EMMI, the Grant No. ERC-AdG-290623, the FWF through Erwin-Schrödinger-Stipendium No. J3507-N27, the Studienstiftung des deutschen Volkes, the DFG through Grant No. STR 1462/1-1, and in part by the Office of Nuclear Physics in the US Department of Energy's Office of Science under Contract No. DE-AC02-05CH11231.

APPENDIX A: GLUON MASS GAP AND IRREGULARITIES

In this section we illustrate the arguments from Sec. III. We restrict ourselves to the case of vanishing background fields. We first show that the infrared behavior of the scaling propagators generically induce a mass gap. We then demonstrate that the decoupling solution necessitates irregular vertices for a mass gap generation due to the infrared finiteness of the decoupling propagators. In Appendix B we show that the vertex irregularities required for a decoupling mass gap cannot be of diagrammatic origin.

A rather general comment is in place here: When one is dealing with the gluon mass gap, it is crucial to carefully take the vanishing momentum limit. In the FRG approach this also means that one must first take the limit $k \to 0$ and then $p \to 0$.

1. Scaling solution

The infrared-relevant part of the self-energy contribution of the ghost loop to the inverse gluon propagator is given by

$$[\Gamma^{(2),\text{gh-loop}}_{AA}]_{\mu\nu}(p) \propto \int_\epsilon^\Lambda \mathrm{d}q \int_{-1}^1 \mathrm{d}t\, q^3 \sqrt{1-t^2} \cdot \frac{q_\mu}{(q^2)^{1+\kappa}} \frac{(q+p)_\nu}{((q+p)^2)^{1+\kappa}}, \tag{A1}$$

where we inserted the infrared ghost propagator from (23) and a classical ghost-gluon vertex, i.e. $[\Gamma^{(3)}_{A\bar{c}c}]^{abc}_\mu(p,q) = \mathrm{i} f^{abc} q_\mu$. Ignoring the angular integration in (A1) for the moment and setting $p = 0$, we find

$$[\Gamma^{(2),\text{gh-loop}}_{AA}]_{\mu\nu}(p) \propto \int_\epsilon^\Lambda \mathrm{d}q\, q_\mu q_\nu q^{-1-4\kappa}, \tag{A2}$$

which is infrared-divergent with $\epsilon^{2-4\kappa}$ if $\kappa > 0.5$. This has to be the case in order to obtain a divergent gluon mass gap consistent with (23). To investigate the mass gap, we project (A1) with $\frac{1}{3}\Pi^\perp_{\mu\nu}(p) - \Pi^{\mathrm{L}}_{\mu\nu}(p)$, where the factor $\frac{1}{3}$ accounts for the three modes of the transverse projection operator. We obtain

$$[\Gamma^{(2),\text{gh-loop}}_{AA,\perp} - \Gamma^{(2),\text{gh-loop}}_{AA,L}](p) \propto \int_0^\Lambda \mathrm{d}q \int_{-1}^1 \mathrm{d}t \frac{q^5}{3} \sqrt{1-t^2} \times \frac{1 - 4t^2 - \frac{|p|}{|q|} t}{(q^2)^{1+\kappa} \cdot ((q+p)^2)^{1+\kappa}}. \tag{A3}$$

One can easily show numerically that the above integral does not vanish in the limit $p \to 0$, but diverges with $(p^2)^{1-2\kappa}$.

2. Decoupling solution

Using again the ghost-loop diagram as an example, we show that a decoupling gluon mass gap requires irregular vertices. We choose the ghost-loop diagram since the ghost-gluon vertex has the smallest tensor space of all vertices,

which makes the example easy to comprehend. We checked explicitly that a similar analysis can be carried out for all diagrams and vertices contributing to the inverse gluon propagator. This can be most easily done by assuming regular vertices (which allows to set $p = 0$) and then showing that the mass gap is zero.

To make this point absolutely clear, we demonstrate this argument for two different tensor bases, for the basis from Sec. III and for one with an explicit splitting into transverse and longitudinal tensors. The former basis, given in (18), reads

$$[\Gamma^{(3)}_{A\bar{c}c}]^{abc}_{\mu}(p,q) = \mathrm{i}f^{abc}(q_\mu Z_{A\bar{c}c,\mathrm{cl}}(p,q) + p_\mu Z_{A\bar{c}c,\mathrm{ncl}}(p,q)), \tag{A4}$$

where p is the gluon and q the antighost momentum. We assume that the ghost-gluon vertex is regular. Therefore the second tensor structure has to be less divergent than $1/|p|$ in the limit of vanishing gluon momentum, i.e.,

$$\lim_{|p|\to 0} |p| Z_{A\bar{c}c,\mathrm{ncl}}(q,p) = 0. \tag{A5}$$

Note that logarithmic divergences, which for example occur in the classical tensor structure of the three-gluon vertex and the nonclassical tensor structures of the four-gluon vertex, do not suffice to violate their respective equivalents of (A5). Utilizing the finiteness of the ghost dressing function and (A5), we can take the limit $|p| \to 0$ to obtain the mass gap contribution of the ghost loop diagram:

$$\begin{aligned} k\partial_k(m^2_{\text{gh-loop},\perp} - m^2_{\text{gh-loop,L}}) &\propto \int_{-1}^{1} \mathrm{d}t\sqrt{1-t^2}\cdot(1-4t^2) Z_{A\bar{c}c,\mathrm{cl}}(0,|q|,t) \\ &\quad \times Z_{A\bar{c}c,\mathrm{cl}}(0,|q|,-t), \end{aligned} \tag{A6}$$

where $\theta = \arccos(t)$ is the angular variable between the loop momentum and the gluon momentum that is taken to zero. The dressing $Z_{A\bar{c}c,\mathrm{cl}}(0,|q|,t)$ is independent of the angular variable t if the ghost-gluon vertex is regular. Thus, the mass gap contribution evaluates to zero:

$$\int_{-1}^{1} \mathrm{d}t\sqrt{1-t^2}(1-4t^2) = 0.$$

Hence, a gluon mass gap requires irregular vertices in the case of the decoupling solution.

Since we consider differences between the vanishing longitudinal and the transverse mass, it might seem more appropriate to split the tensor basis of the ghost-gluon vertex into a purely longitudinal and a purely transverse part. We show now that this leads to the same conclusion. Transverse and longitudinal projection of the classical tensor structure already gives us a complete orthogonal basis:

$$\begin{aligned} [\Gamma^{(3)}_{A\bar{c}c}]^{abc}_{\mu}(p,q) = \mathrm{i}f^{abc}[&\Pi^{\perp}_{\mu\nu}(p) q_\nu Z_{A\bar{c}c,\perp}(p,q) \\ &+ \Pi^{\mathrm{L}}_{\mu\nu}(p) q_\nu Z_{A\bar{c}c,\mathrm{L}}(p,q)], \end{aligned} \tag{A7}$$

where p is the gluon and q the antighost momentum. The projection operators are given by $\Pi^{\mathrm{L}}_{\mu\nu}(p) = p_\mu p_\nu / p^2$ and $\Pi^{\perp}_{\mu\nu}(p) = \mathbb{1}_{\mu\nu} - \Pi^{\mathrm{L}}_{\mu\nu}(p)$. Note that the basis (A7) contains a discontinuity at $p = 0$ due to the projection operators. The mass gap contribution of the ghost diagram with this ghost-gluon vertex basis evaluates to

$$\begin{aligned} k\partial_k(m^2_{\text{gh-loop},\perp} - m^2_{\text{gh-loop,L}}) \propto \int_{-1}^{1} \mathrm{d}t\sqrt{1-t^2} \\ \cdot \left(\frac{1-t^2}{3} Z_{A\bar{c}c,\perp}(0,|q|,t) Z_{A\bar{c}c,\perp}(0,|q|,-t) \right. \\ \left. - t^2 Z_{A\bar{c}c,\mathrm{L}}(0,|q|,t) Z_{A\bar{c}c,\mathrm{L}}(0,|q|,-t) \right). \end{aligned} \tag{A8}$$

Regularity (A5), implies a degenerate tensor space in the limit of vanishing gluon momentum. The ghost-gluon vertex can then be fully described by $Z_{A\bar{c}c,\mathrm{cl}}(0,|q|) \equiv Z_{A\bar{c}c,\mathrm{L}}(0,|q|,t)$. Using the identity $\mathbb{1}_{\mu\nu} = \Pi^{\perp}_{\mu\nu}(p) + \Pi^{\mathrm{L}}_{\mu\nu}(p)$, we find

$$Z_{A\bar{c}c,\mathrm{cl}}(0,|q|) = Z_{A\bar{c}c,\perp}(0,|q|) = Z_{A\bar{c}c,\mathrm{L}}(0,|q|). \tag{A9}$$

Using (A9) we can perform the angular integration in (A8) and find that the mass gap contribution vanishes.

We want to stress that this statement is general and holds for any diagrammatic method. For example, the same conclusion can be drawn for the ghost-loop diagram of the gluon propagator Dyson-Schwinger equation that is also proportional to (A6) or (A8). Consequently, for the decoupling solution there can be no mass gap with regular vertices.

APPENDIX B: GHOST-TRIANGLE

In Appendix A it is shown that the decoupling solution requires irregular vertices. In the three gluon vertex, this irregularity has to occur if one momentum is sent to zero while the others are nonvanishing. Those vertex irregularities can be generated either by back-coupling of momentum dependence or by diagrammatic infrared singularities. We cannot observe the former in our computation of the purely transverse system. To investigate the latter case we use that the gluonic diagrams decouple from the infrared dynamics due to the gluon mass gap. Therefore we can focus on the ghost loops as possible sources of diagrammatic IR irregularities without loss of generality. The ghost-gluon vertex as well as the ghost propagator are constant and finite in the infrared. In the following we show explicitly that the three-gluon vertex does not obtain an irregular contribution from the ghost triangle. Its relevant part is given by

$$[\Gamma^{(3),\text{gh-loop}}_{A^3}]_{\mu\nu\rho}(p,q,r) \propto \int \frac{\mathrm{d}^d l}{(2\pi)^d} \frac{(l+p)_\mu}{(l+p)^2} \frac{l_\nu}{l^2} \frac{(l-q)_\rho}{(l-q)^2}. \tag{B1}$$

To confirm that (B1) does not generate an irregularity in the limit $\frac{|p|}{|q|} \to 0$, we consider the low and high momentum integration regions separately. If the loop momentum $|l|$ is of the order of $|q|$, then $|p| \ll |l|$ and the p dependence in (B1) is suppressed. Thus no irregular structure can be generated from this integration region. For small loop momenta $|l| \approx |p|$ we have $|l| \ll |q|$ and the contribution to the integral in the limit $\frac{|p|}{|l|} \to 0$ is given by

$$\frac{q_\rho}{q^2} \int \frac{\mathrm{d}^d l}{(2\pi)^d} \frac{(l+p)_\mu}{(l+p)^2} \frac{l_\nu}{l^2}. \tag{B2}$$

This integral can easily be solved analytically for $d = 4 - 2\epsilon$ to show that it has no irregularities, which one also expects from a dimensional analysis of (B2). Hence, we conclude, that the decoupling ghost triangle cannot generate the irregularity necessary for the dynamical generation of a gluon mass gap. Note that the ghost triangle develops a nontrivial pole structure in the case of the scaling solution, see [99]. We have verified these findings numerically, and since they are in accordance with perturbation theory, we expect similar arguments to hold for the ghost loops contributing to higher n-point functions.

APPENDIX C: NUMERICAL IMPLEMENTATION

The algebraic flow equations are derived using DoFun [100]. The projected flow equations are then traced using the *FormTracer* [101], a *Mathematica* package that uses FORM [102,103]. The output is exported as optimized C code with FORMs optimization algorithm [104]. The calculation is performed with the *frgsolver*, a flexible, object-orientated, parallelized C++ framework developed by the fQCD collaboration [34], whose development was initiated in [1]. The framework uses the adaptive ordinary differential equation solver from the BOOST libraries [105], the Eigen linear algebra library [106] and an adaptive multidimensional integration routine from [107] which implements [108,109] to solve the integro-differential equations.

APPENDIX D: TENSOR STRUCTURES OF YM-VERTICES

In this section we define our conventions for the tensor structures in which we expanded our vertices and the used projections. The tensor structures for the classical YM three-point vertices are defined by

$$\begin{aligned}[\mathcal{T}_{A^3,\text{cl}}]^{abc}_{\mu\nu\rho}(p,q) &= \mathrm{i} f^{abc}\{(p-q)_\rho \delta_{\mu\nu} + \text{perm}\},\\ [\mathcal{T}_{A\bar{c}c,\text{cl}}]^{abc}_{\mu}(p,q) &= \mathrm{i} f^{abc} q_\mu,\end{aligned} \tag{D1}$$

and by

$$[\mathcal{T}_{A^4,\text{cl}}]^{abcd}_{\mu\nu\rho\sigma}(p,q,r) = f^{abn} f^{cdn} \delta_{\mu\rho}\delta_{\nu\sigma} + \text{perm}, \tag{D2}$$

for the four-point function. For the transversally projected ghost-gluon vertex this single tensor constitutes already a full basis and the projection is uniquely defined. However, additional allowed tensors exist in the case of the three-gluon and four-gluon vertices. We obtained the dressing functions by contracting the equations with

$$\Pi^{\perp}_{\mu\bar{\mu}}(p)\Pi^{\perp}_{\nu\bar{\nu}}(q)\Pi^{\perp}_{\rho\bar{\rho}}(p+q)[\mathcal{T}_{A^3,\text{cl}}]^{abc}_{\bar{\mu}\bar{\nu}\bar{\rho}}(p,q), \tag{D3}$$

and

$$\Pi^{\perp}_{\mu\bar{\mu}}(p)\Pi^{\perp}_{\nu\bar{\nu}}(q)\Pi^{\perp}_{\rho\bar{\rho}}(r)\Pi^{\perp}_{\sigma\bar{\sigma}}(p+q+r)[\mathcal{T}_{A^4,\text{cl}}]^{abcd}_{\bar{\mu}\bar{\nu}\bar{\rho}\bar{\sigma}}(p,q,r), \tag{D4}$$

respectively.

APPENDIX E: REGULATORS

In the functional renormalization group, the choice of the regulator, together with the choice of the cutoff-independent parts of the initial effective action corresponds to defining a renormalization scheme, for a more detailed discussion see [5]. Moreover, to any given order of a given approximation scheme there exist optimized regulators that lead to the most rapid convergence of the results, hence minimizing the systematic error, see [5,26,27]. For recent extensions and applications relevant for the present work see [28,29]. In the present work we use

$$\begin{aligned}R^{ab}_{k,\mu\nu}(p) &= \tilde{Z}_{A,k} r(p^2/k^2) p^2 \delta^{ab} \Pi^{\perp}_{\mu\nu}(p),\\ R^{ab}_{k}(p) &= \tilde{Z}_{c,k} r(p^2/k^2) p^2 \delta^{ab},\end{aligned} \tag{E1}$$

for the gluon and the ghost fields, respectively. For the shape function we choose a smooth version of the Litim or flat regulator [26]:

$$r(x) = \left(\frac{1}{x} - 1\right) \cdot \frac{1}{1 + e^{\frac{x-1}{a}}}, \tag{E2}$$

where we set $a = 0.02$. It has been argued in [5] that smooth versions of the flat regulator satisfy the functional optimization criterion put forward there.

In (E1) we multiply the regulators with scaling factors $\tilde{Z}$, related to the corresponding wave function renormalizations of the gluon and ghost fields

$$\tilde{Z}_{A,k} := Z_{A,k}((k^n + \bar{k}^n)^{1/n}),$$
$$\tilde{Z}_{c,k} := Z_{c,k}(k), \tag{E3}$$

where we choose $n \approx 6$ and $\bar{k} \approx 1$ GeV. The cutoff scale running of $\tilde{Z}_A$ is held constant below scales of about 1 GeV as the gluon wave function renormalization $Z_{A,k}(p \approx k)$ diverges for $k \to 0$. Separating the tensor structure by

$$[\Gamma^{(2)}_{AA}]^{ab}_{\mu\nu}(p) =: \Gamma^{(2)}_{AA,k}(p)\delta^{ab}\Pi^{\perp}_{\mu\nu}(p), \tag{E4}$$

we parametrize $\Gamma^{(2)}_{AA,k}(p)$ by

$$\begin{aligned}\Gamma^{(2)}_{AA,k}(p) &=: Z_{A,k}(p) \cdot p^2 \\ &=: \bar{Z}_{A,k}(p) \cdot p^2 + m_k^2 \\ &=: \hat{Z}_{A,k}(p) \cdot (p^2 + m_k^2),\end{aligned} \tag{E5}$$

where we define $m_k^2 := \Gamma^{(2)}_{AA,k}(0)$ to guarantee the uniqueness of $\hat{Z}_{A,k}$. We see that these choices differ considerably below 1 GeV. For more details see Fig. 10 (right panel). In particular the naive choice $Z_{A,k}$ diverges since it carries the gluon mass gap. Consequently, we freeze $Z_{A,k}$ at a scale $\bar{k}$ close to 1 GeV. We have checked explicitly that varying the value of $\bar{k}$ and n has no influence on our results.

APPENDIX F: SCALE SETTING AND NORMALIZATION

When comparing to lattice results, the momentum scales as well as the global normalizations of the fields have to be fixed. We set the scale by

$$p_{\mathrm{GeV}} = c \cdot p_{\mathrm{internal}},$$

where we choose c such that the scale of the maximum of the gluon dressing $1/Z_A(p)$ agrees with the lattice scale from [79], which lies at $p \approx 0.955$ GeV.

We then rescale the gluon dressing by $Z_A^{-1}(p) \to aZ_A^{-1}(p)$ with a chosen such that it minimizes

$$\begin{aligned}N_{Z_A}(a) = \sum_i \frac{\Delta x_i}{\Delta E_i^2} \cdot [&(aZ_A^{-1}(p_i) - Z_A^{L,-1}(p_i))^2 \\ &+ (a\partial_p Z_A^{-1}(p_i) - \partial_p Z_A^{L,-1}(p_i))^2],\end{aligned} \tag{F1}$$

where we sum over all lattice points that fulfill $0.8\ \mathrm{GeV} \le p_i \le 4\ \mathrm{GeV}$. We do not include points with smaller momenta since they can be affected by the global gauge fixing procedure. Points with momentum larger than 4 GeV are also not included since they might contain finite volume effects. In (F1), we weight the lattice points with $\Delta x_i/\Delta E_i^2$, where Δx_i denotes the distance to the next point and ΔE_i is the statistical error of the point. The superscript L in (F1) marks lattice dressing functions. The ghost dressing is rescaled analogously.

[1] M. Mitter, J. M. Pawlowski, and N. Strodthoff, Phys. Rev. D **91**, 054035 (2015).
[2] J. Berges, N. Tetradis, and C. Wetterich, Phys. Rep. **363**, 223 (2002).
[3] C. D. Roberts and S. M. Schmidt, Prog. Part. Nucl. Phys. **45**, S1 (2000).
[4] R. Alkofer and L. von Smekal, Phys. Rep. **353**, 281 (2001).
[5] J. M. Pawlowski, Ann. Phys. (Amsterdam) **322**, 2831 (2007).
[6] C. S. Fischer, J. Phys. G **32**, R253 (2006).
[7] H. Gies, Lect. Notes Phys. **852**, 287 (2012).
[8] B.-J. Schaefer and J. Wambach, Phys. Part. Nucl. **39**, 1025 (2008).
[9] C. S. Fischer, A. Maas, and J. M. Pawlowski, Ann. Phys. (Amsterdam) **324**, 2408 (2009).
[10] D. Binosi and J. Papavassiliou, Phys. Rep. **479**, 1 (2009).
[11] J. Braun, J. Phys. G **39**, 033001 (2012).
[12] A. Maas, Phys. Rep. **524**, 203 (2013).
[13] H. Sanchis-Alepuz and R. Williams, J. Phys. Conf. Ser. **631**, 012064 (2015).
[14] U. Ellwanger, M. Hirsch, and A. Weber, Z. Phys. C **69**, 687 (1996).
[15] L. von Smekal, R. Alkofer, and A. Hauck, Phys. Rev. Lett. **79**, 3591 (1997).
[16] B. Bergerhoff and C. Wetterich, Phys. Rev. D **57**, 1591 (1998).
[17] H. Gies, Phys. Rev. D **66**, 025006 (2002).
[18] J. M. Pawlowski, D. F. Litim, S. Nedelko, and L. von Smekal, Phys. Rev. Lett. **93**, 152002 (2004).
[19] C. S. Fischer and R. Alkofer, Phys. Rev. D **67**, 094020 (2003).
[20] C. S. Fischer and H. Gies, J. High Energy Phys. 10 (2004) 048.
[21] A. C. Aguilar, D. Binosi, and J. Papavassiliou, Phys. Rev. D **78**, 025010 (2008).
[22] P. Boucaud, J. P. Leroy, A. Le Yaouanc, J. Micheli, O. Pène, and J. Rodríguez-Quintero, J. High Energy Phys. 06 (2008) 099.
[23] M. Tissier and N. Wschebor, Phys. Rev. D **82**, 101701 (2010).
[24] M. Q. Huber, Phys. Rev. D **93**, 085033 (2016).
[25] C. Feuchter and H. Reinhardt, Phys. Rev. D **70**, 105021 (2004).
[26] D. F. Litim, Phys. Lett. B **486**, 92 (2000).

[27] D. F. Litim, Phys. Rev. D **64**, 105007 (2001).
[28] D. Schnoerr, I. Boettcher, J. M. Pawlowski, and C. Wetterich, Ann. Phys. (Amsterdam) **334**, 83 (2013).
[29] J. M. Pawlowski, M. M. Scherer, R. Schmidt, and S. J. Wetzel, arXiv:1512.03598.
[30] L. Fister and J. M. Pawlowski (unpublished).
[31] A. J. Helmboldt, J. M. Pawlowski, and N. Strodthoff, Phys. Rev. D **91**, 054010 (2015).
[32] J. Braun, L. Fister, J. M. Pawlowski, and F. Rennecke, Phys. Rev. D **94**, 034016 (2016).
[33] F. Rennecke, Phys. Rev. D **92**, 076012 (2015).
[34] J. Braun, A. K. Cyrol, L. Fister, W.-J. Fu, T. K. Herbst, M. Mitter, J. M. Pawlowski, F. Rennecke, and N. Strodthoff (fQCD Collaboration) (unpublished).
[35] C. Wetterich, Phys. Lett. B **301**, 90 (1993).
[36] L. Fister and J. M. Pawlowski, arXiv:1112.5440.
[37] L. Fister and J. M. Pawlowski, Phys. Rev. D **88**, 045010 (2013).
[38] G. Eichmann, R. Williams, R. Alkofer, and M. Vujinovic, Phys. Rev. D **89**, 105014 (2014).
[39] A. K. Cyrol, M. Q. Huber, and L. von Smekal, Eur. Phys. J. C **75**, 102 (2015).
[40] A. K. Cyrol, Master's thesis, Darmstadt University of Technology, 2014.
[41] C. Kellermann and C. S. Fischer, Phys. Rev. D **78**, 025015 (2008).
[42] D. Binosi, D. Ibáñez, and J. Papavassiliou, J. High Energy Phys. 09 (2014) 059.
[43] J. A. Gracey, Phys. Rev. D **90**, 025011 (2014).
[44] M. Q. Huber and L. von Smekal, J. High Energy Phys. 04 (2013) 149.
[45] A. C. Aguilar, D. Ibáñez, and J. Papavassiliou, Phys. Rev. D **87**, 114020 (2013).
[46] M. Pelaez, M. Tissier, and N. Wschebor, Phys. Rev. D **88**, 125003 (2013).
[47] A. Blum, M. Q. Huber, M. Mitter, and L. von Smekal, Phys. Rev. D **89**, 061703 (2014).
[48] J. Gracey, Phys. Rev. D **90**, 025014 (2014).
[49] M. Q. Huber, D. R. Campagnari, and H. Reinhardt, Phys. Rev. D **91**, 025014 (2015).
[50] R. Williams, C. S. Fischer, and W. Heupel, Phys. Rev. D **93**, 034026 (2016).
[51] U. Ellwanger, Phys. Lett. B **335**, 364 (1994).
[52] M. D'Attanasio and T. R. Morris, Phys. Lett. B **378**, 213 (1996).
[53] Y. Igarashi, K. Itoh, and H. So, Prog. Theor. Phys. **106**, 149 (2001).
[54] Y. Igarashi, K. Itoh, and J. M. Pawlowski, arXiv: 1604.08327.
[55] L. von Smekal, K. Maltman, and A. Sternbeck, Phys. Lett. B **681**, 336 (2009).
[56] J. Braun, H. Gies, and J. M. Pawlowski, Phys. Lett. B **684**, 262 (2010).
[57] F. Marhauser and J. M. Pawlowski, arXiv:0812.1144.
[58] J. Braun, L. M. Haas, F. Marhauser, and J. M. Pawlowski, Phys. Rev. Lett. **106**, 022002 (2011).
[59] J. Braun, A. Eichhorn, H. Gies, and J. M. Pawlowski, Eur. Phys. J. C **70**, 689 (2010).
[60] D. Dudal, S. Sorella, N. Vandersickel, and H. Verschelde, Phys. Rev. D **77**, 071501 (2008).
[61] D. Dudal, J. A. Gracey, S. P. Sorella, N. Vandersickel, and H. Verschelde, Phys. Rev. D **78**, 065047 (2008).
[62] D. Dudal, S. Sorella, N. Vandersickel, and H. Verschelde, Phys. Rev. D **79**, 121701 (2009).
[63] D. Dudal, S. Sorella, and N. Vandersickel, Phys. Rev. D **84**, 065039 (2011).
[64] M. A. L. Capri, D. Dudal, D. Fiorentini, M. S. Guimaraes, I. F. Justo, A. D. Pereira, B. W. Mintz, L. F. Palhares, R. F. Sobreiro, and S. P. Sorella, Phys. Rev. D **92**, 045039 (2015).
[65] D. Zwanziger, Phys. Rev. D **65**, 094039 (2002).
[66] C. Lerche and L. von Smekal, Phys. Rev. D **65**, 125006 (2002).
[67] C. S. Fischer, R. Alkofer, and H. Reinhardt, Phys. Rev. D **65**, 094008 (2002).
[68] R. Alkofer, C. S. Fischer, and F. J. Llanes-Estrada, Phys. Lett. B **611**, 279 (2005).
[69] C. S. Fischer and J. M. Pawlowski, Phys. Rev. D **75**, 025012 (2007).
[70] R. Alkofer, M. Q. Huber, and K. Schwenzer, Phys. Rev. D **81**, 105010 (2010).
[71] C. S. Fischer and J. M. Pawlowski, Phys. Rev. D **80**, 025023 (2009).
[72] J. M. Cornwall, Phys. Rev. D **26**, 1453 (1982).
[73] T. Kugo and I. Ojima, Prog. Theor. Phys. Suppl. **66**, 1 (1979).
[74] G. K. Savvidy, Phys. Lett. **71B**, 133 (1977).
[75] A. Eichhorn, H. Gies, and J. M. Pawlowski, Phys. Rev. D **83**, 045014 (2011).
[76] A. C. Aguilar, D. Binosi, and J. Papavassiliou, Phys. Rev. D **84**, 085026 (2011).
[77] A. C. Aguilar, D. Ibáñez, V. Mathieu, and J. Papavassiliou, Phys. Rev. D **85**, 014018 (2012).
[78] C. T. Figueiredo and A. C. Aguilar, J. Phys. Conf. Ser. **706**, 052007 (2016).
[79] A. Sternbeck, E. M. Ilgenfritz, M. Muller-Preussker, A. Schiller, and I. L. Bogolubsky, *Proc. Sci.*, LAT2006 (2006) 076, [arXiv:hep-lat/0610053].
[80] A. Cucchieri and T. Mendes, Phys. Rev. Lett. **100**, 241601 (2008).
[81] A. Cucchieri and T. Mendes, Phys. Rev. D **78**, 094503 (2008).
[82] A. Maas, J. M. Pawlowski, D. Spielmann, A. Sternbeck, and L. von Smekal, Eur. Phys. J. C **68**, 183 (2010).
[83] A. Maas, Phys. Lett. B **689**, 107 (2010).
[84] A. Sternbeck and M. Müller-Preussker, Phys. Lett. B **726**, 396 (2013).
[85] A. Maas, Phys. Rev. D **93**, 054504 (2016).
[86] A. G. Duarte, O. Oliveira, and P. J. Silva, Phys. Rev. D **94**, 014502 (2016).
[87] A. Aguilar, D. Binosi, D. Ibáñez, and J. Papavassiliou, Phys. Rev. D **89**, 085008 (2014).
[88] R. Williams, Eur. Phys. J. A **51**, 57 (2015).
[89] M. Q. Huber (private communication).
[90] R. Williams (private communication).
[91] M. Q. Huber and L. von Smekal, J. High Energy Phys. 06 (2014) 015.
[92] M. Pelez, M. Tissier, and N. Wschebor, Phys. Rev. D **90**, 065031 (2014).
[93] A. Cucchieri, A. Maas, and T. Mendes, Phys. Rev. D **74**, 014503 (2006).

[94] A. Cucchieri, A. Maas, and T. Mendes, Phys. Rev. D **77**, 094510 (2008).
[95] A. Maas (to be published).
[96] A. Cucchieri, T. Mendes, O. Oliveira, and P. J. Silva, Phys. Rev. D **76**, 114507 (2007).
[97] A. Sternbeck, L. von Smekal, D. B. Leinweber, and A. G. Williams, *Proc. Sci.*, LAT2007 (2007) 340 [arXiv:0710.1982].
[98] A. K. Cyrol, M. Mitter, J. M. Pawlowski and N. Strodthoff (to be published).
[99] R. Alkofer, M. Q. Huber, and K. Schwenzer, Eur. Phys. J. C **62**, 761 (2009).
[100] M. Q. Huber and J. Braun, Comput. Phys. Commun. **183**, 1290 (2012).
[101] A. K. Cyrol, M. Mitter, J. M. Pawlowski and N. Strodthoff (to be published).
[102] J. Vermaseren, arXiv:math-ph/0010025.
[103] T. van Ritbergen, A. N. Schellekens, and J. A. M. Vermaseren, Int. J. Mod. Phys. A **14**, 41 (1999).
[104] J. Kuipers, T. Ueda, and J. A. M. Vermaseren, Comput. Phys. Commun. **189**, 1 (2015).
[105] K. Ahnert and M. Mulansky, http://www.boost.org/doc/libs/1_60_0/libs/numeric/odeint/doc/html/index.html.
[106] G. Guennebaud and B. Jacob, Eigen v3 (linear algebra library) http://eigen.tuxfamily.org.
[107] S. G. Johnson, http://ab-initio.mit.edu/wiki/index.php/Cubature.
[108] J. Berntsen, T. O. Espelid, and A. Genz, ACM Trans. Math. Softw. **17**, 437 (1991).
[109] A. C. Genz and A. Malik, J. Comput. Appl. Math. **6**, 295 (1980).